

JUL 23 1998

# **MIXED-MODE FRACTURE OF SOLID PROPELLANTS**

Final Technical Report to the

**AIR FORCE OFFICE OF SCIENTIFIC RESEARCH**

Professor K. Ravi-Chandar

July 15, 1998

Grant Number F49620-96-1-0139

**UNIVERSITY OF HOUSTON  
HOUSTON, TX 77204**

19980824 188

DTIC QUALITY INSPECTED Y

# REPORT DOCUMENTATION PAGE

Public reporting burden for this collection of information is estimated to average 1 hour per response, including the time for reviewing instructions, searching existing data sources, gathering the data needed, and completing and reviewing this collection of information. Send comments regarding this burden estimate or any other aspect of this collection of information, including suggestions for reducing this burden to Washington Headquarters Services, Directorate for Information Operations and Reports, 1215 Jefferson Davis Highway, Suite 1204, Arlington, VA 22202-4302, and to the Office of Management and Budget, Paperwork Reduction Project (0704-0188), Washington, DC 20503.

AFRL-SR-BL-TR-98-

0583

<b>1. AGENCY USE ONLY (Leave blank)</b>		<b>2. REPORT DATE</b> July 15, 1998	<b>3. REPORT TYPE AND DATES COVERED</b> Final Report; 5/1/96 to 4/30/98	
<b>4. TITLE AND SUBTITLE</b> Mixed-mode fracture of solid propellants			<b>5. FUNDING NUMBERS</b> F49620-96-1-0139	
<b>6. AUTHOR(S)</b> Professor K. Ravi-Chandar				
<b>7. PERFORMING ORGANIZATION NAME(S) AND ADDRESS(ES)</b> University of Houston 4800 Calhoun Blvd Houston, TX 77204			<b>8. PERFORMING ORGANIZATION REPORT NUMBER</b>	
<b>9. SPONSORING / MONITORING AGENCY NAME(S) AND ADDRESS(ES)</b> Air Force Office of Scientific Research Mechanics and Materials Program 110 Duncan Ave, Room Bolling AFB, DC 20332-8080 NA			<b>10. SPONSORING / MONITORING AGENCY REPORT NUMBER</b>	
<b>11. SUPPLEMENTARY NOTES</b>				
<b>12a. DISTRIBUTION / AVAILABILITY STATEMENT</b> This document has been approved for public release and sale; distribution unlimited				<b>12b. DISTRIBUTION CODE</b>
<b>13. ABSTRACT (Maximum 200 Words)</b> This report describes an investigation into the mixed-mode fracture behavior of solid propellants. Experiments were performed at different mixed mode loading conditions at different temperatures and strain rates. The collection of data suggested that while the maximum tangential stress criterion was a reasonable indicator of the onset of crack initiation, the crack growth direction was not well predicted, primarily due to the development of damage near the crack tip. In an effort to overcome this limitation, a cohesive zone damage model was introduced to represent the crack. This model was then embedded in a boundary element method so that arbitrary crack growth under mixed mode loading can be simulated. The details of both the cohesive zone representation and the boundary element implementation are provided. Comparison of the predictions from the stress intensity factor based fracture criterion and cohesive zone model based simulation is presented.				
<b>14. SUBJECT TERMS</b>			<b>15. NUMBER OF PAGES</b> 38	
			<b>16. PRICE CODE</b>	
<b>17. SECURITY CLASSIFICATION OF REPORT</b> Unclassified	<b>18. SECURITY CLASSIFICATION OF THIS PAGE</b> Unclassified	<b>19. SECURITY CLASSIFICATION OF ABSTRACT</b> Unclassified	<b>20. LIMITATION OF ABSTRACT</b>	

## **Abstract**

This report describes an investigation into the mixed-mode fracture behavior of solid propellants. Experiments were performed at different mixed mode loading conditions at different temperatures and strain rates. The collection of data suggested that while the maximum tangential stress criterion was a reasonable indicator of the onset of crack initiation, the crack growth direction was not well predicted, primarily due to the development of damage near the crack tip. In an effort to overcome this limitation, a cohesive zone damage model was introduced to represent the crack. This model was then embedded in a boundary element method so that arbitrary crack growth under mixed mode loading can be simulated. The details of both the cohesive zone representation and the boundary element implementation are provided. Comparison of the predictions from the stress intensity factor based fracture criterion and cohesive zone model based simulation is presented.

## TABLE OF CONTENTS

Abstract	ii
List of figures	iv
1. Introduction	1
2. Experiments on the mixed mode fracture of solid propellants	2
3. Cohesive zone model for a crack in elastostatics	3
4. Boundary integral formulation of the elastostatic crack problem with a cohesive zone tip.	6
4.1. Summary of the dual integral equations for a simple structure	7
4.2. Single-domain dual integral equations for a cracked structure	8
4.3. Iterative boundary element method of successive over-relaxation	12
5. Applications	16
5.1. Single edge crack under tension	17
5.2. Interaction of cracks in the double edge cracked specimen	18
6. Mixed-mode fracture with a cohesive zone	19
7. Conclusions	20
8. References	20

## LIST OF FIGURES

Figure 1.	Mixed-mode loading geometry and grip attachments.	22
Figure 2.	Failure interaction curve showing critical values of the mode-I and mode II stress intensity factors at crack initiation. The prediction of the MTS theory is also indicated.	22
Figure 3.	Dependence of the mode-I fracture toughness on the loading rate.	23
Figure 4.	Measured variation of the crack kinking angle with the mode mixity parameter $\delta = \mu/(1+\mu)$ . Predictions of the MTS theory do not correspond to the experimental observations.	23
Figure 5.	(a) Illustration of the two originally coincident points of a cohesive zone in the opening mode, connected by the line spring; (b) schematic diagram of the constitutive law of the line spring in terms of the traction and displacement jump. Note that instantaneous loading and unloading of the line spring is given by the slope $k$ .	24
Figure 6.	(a) Illustration of the two originally coincident points of a cohesive zone in the contact/sliding mode. The tangential interaction between the two points is modeled using Coulomb frictional force and the cohesive force if the cohesive line spring is not already broken; (b) sketch of the variation of the frictional coefficient of the contact surface.	24
Figure 7.	An isotropic, homogeneous, linear elastic domain $\Omega$ with boundary $\Gamma$ .	25
Figure 8.	A domain $\Omega$ containing a crack $\Gamma^c$ is cut into two subdomains $\Omega_I$ and $\Omega_{II}$ along the dotted line path $\Gamma^a$ .	25
Figure 9.	The discretization of the boundary into elements is shown in this figure. Each element contains one or more nodes distributed uniformly within the element. The nodes are internal to the element, indicating discontinuous elements.	26
Figure 10.	The two-parameter constitutive law for the cohesive zone material used in the simulations.	26
Figure 11.	The configuration of a rectangular specimen with a single edge crack of initial length $a_0$ , under displacement controlled elongation. This initial crack is parallel to the loading boundaries, and may be offset from the symmetry line in a distance.	27
Figure 12.	Load-elongation diagram of a set of simulations with a crack initially lying on $x_2 = 0$ and with a length $a_0$ from 0.03, to 0.78. An initial cohesive zone of size 0.02 is assumed in all the simulations. The crack growth is in the pure mode I. For $a_0 < 0.48$ approximately, crack extension is unstable under displacement control.	27
Figure 13.	Crack opening profiles at the critical point of instability in two of the simulations for $a_0 = 0.03$ and 0.18.	28

Figure 14.	Traction normal component $p_n$ along the cohesive zone at the critical point of instability in four of the simulations for $a_0 = 0.03, 0.08, 0.13$ , and $0.18$ . The tangential component is zero indicating a pure opening mode for the cohesive zone. Note that, for very short initial crack lengths, the cohesive zones are not fully developed.	28
Figure 15.	Crack trajectories in the simulations with different offsets of initial cracks. Nodes along the newly-created cracks are indicative of the new crack element ends.	29
Figure 16.	The loading configuration of a rectangular specimen with two edge cracks on the opposite sides, under displacement controlled elongation. The cracks are initially parallel to the loading boundaries, and may be offset from the symmetry line by a offset $d_{offset}$ .	29
Figure 17.	Load-elongation curves in the simulations of crack interaction with the offset $d_{offset}$ as given above. Besides, the cracks $a_{10} = a_{20} = 0.28$ initially, and each crack tip was assumed to have an initial cohesive zone of size $0.02$ . The dashed lined indicate the loss of structural stability.	30
Figure 18.	Deformed configuration of the specimen with two edge cracks with the offset $d_{offset} = 0.1$ , corresponding to an extension $\Delta = 0.0038$ .	30
Figure 19.	Deformed configuration of the specimen with two edge cracks with the offset $d_{offset} = 0.2$ , corresponding to an extension $\Delta = 0.0038$ .	31
Figure 20	Load-load point displacement variation for mixed-mode crack growth, showing a comparison of the predictions of LEFM and the cohesive zone model.	31
Figure 21.	Comparison of the crack path predicted by the maximum tangential stress criterion and the cohesive zone model.	32
Figure 22.	Comparison of the crack path predicted by LEFM and the cohesive zone model; only the region near the initial crack is shown.	32

## 1. Introduction

The mixed-mode problem considered here involves determination of the critical conditions at which a crack subjected to a combination of loading modes I and II will initiate. Another important consideration is the crack trajectory upon initiation. Since the early work of Erdogan and Sih (1962), this problem has received considerable attention (for example, Williams and Ewing, (1972); Maiti and Smith (1983), Ueda *et al.*, (1983)) and a number of criteria have been proposed to predict crack initiation behavior under mixed-mode loading. In the two-dimensional case, the Cartesian components of the crack tip stresses can be expressed (in terms of the polar coordinates as)

$$\sigma_{\alpha\beta}(r, \theta) = \frac{K_I}{\sqrt{2\pi r}} f_{\alpha\beta}(\theta) + \frac{K_{II}}{\sqrt{2\pi r}} g_{\alpha\beta}(\theta); \quad r \rightarrow 0, \alpha, \beta = 1, 2, \quad (1)$$

where  $f_{\alpha\beta}(\theta)$  and  $g_{\alpha\beta}(\theta)$  are characteristic functions and  $K_I$  and  $K_{II}$  are the mode I and mode II stress intensity factors respectively. The asymmetry of the loading is generally described in terms of the mixity parameter  $\mu$  which is defined as

$$\mu = \frac{K_{II}}{K_I}. \quad (2)$$

Thus the mixed-mode fracture problem involves determining critical stress intensity factor pairs  $(K_I^c, K_{II}^c)$  for different values of  $\mu$ , at which the crack will initiate. Furthermore it is required to determine the initiation angle  $\gamma$  as a function of  $\mu$ , as well as the subsequent crack propagation path. Many different criteria have been proposed to predict the critical condition for crack initiation and the crack trajectory upon initiation; the maximum tangential stress criterion (MTS) described is probably the most widely used. This criterion was proposed by Erdogan and Sih (1962) and is stated as follows: *Crack extension starts at the crack tip in a radial direction. This extension is in that radial direction perpendicular to the direction of the greatest tension. Crack extension begins when this tension reaches a certain critical value at a certain distance from the crack tip.* Erdogan and Sih (1962) used a plate containing a central crack of length  $2a$  subjected to uniaxial far-field loading  $\sigma$ , the crack being oriented at angle  $\beta$  to the loading direction. They obtained a relation for the initiation angle  $\gamma$  as a function of  $\mu$  by equating the partial derivative  $\partial\sigma_{\theta\theta}/\partial\theta$  to zero (equivalently the shear stress  $\sigma_{r\theta}$  can be equated to zero). Both these conditions yield the relation

$$\sin \gamma + (3 \cos \gamma - 1)\mu = 0. \quad (3)$$

From Eq.(3) it can be shown that for pure mode II conditions ( $\mu = 0$ ) the initiation angle is predicted to be  $70.5^\circ$ .

In the present work, this problem of mixed-mode fracture has been examined for the solid propellant materials which are particulate composites. In characterizing the fracture of solid propellants, theories of linear elastic fracture mechanics (LEFM) and linear and nonlinear vis-

coelastic fracture mechanics (VEFM) are usually applied. The fundamental constitutive assumptions of these theories dictate that the theories will have a certain range of validity depending on the nature of the loading, time scale of application etc. For example, if the loads are applied rapidly, it might be appropriate to use LEFM; on the other hand, under conditions of storage, over long periods of time, viscoelastic deformation dominates and the appropriate theory to use in determining the reliability of the solid propellant would be the VEFM. While these theories are firmly grounded in the classical principles of mechanics, experimental results obtained on solid propellant materials do not appear to correlate well with the predictions of the theory (Francis *et al.*, 1980). The reasons for this disagreement could arise potentially from errors in experimental measurements and in the theoretical interpretation. The measurements typically obtained in the experiments are of the loads and displacements at the boundaries of the specimen. These are then interpreted in terms of the crack tip parameters using LEFM or VEFM assuming, of course, that either of these theories is appropriate. However, there are a number of problems in such an interpretation. Near the crack tip, in a small zone surrounding the crack tip, there exists a zone of large deformations and damage, which cannot be modeled as an elastic or viscoelastic medium.

We report here, the results of an investigation into mixed-mode fracture. In Section 2, the experimental methodology and results on the experimental characterization of mixed-mode fracture are presented. The problems associated with the prediction of mixed mode fracture are described briefly. In an effort to provide a predictive capability for describing mixed-mode fracture, the crack tip process zone is modeled using a cohesive zone description. The idealization of the crack tip processes in terms of the cohesive zone model is described in Section 3. The cohesive zone model may be incorporated into any numerical scheme for generating crack growth computations, but the boundary integral formulation is the most advantageous since it does not require extensive remeshing; the BEM formulation is described in Section 4. Two example problems describing the application of the method to crack growth predictions are described in Section 5 in order to demonstrate the potential of the method. Finally, in Section 6, the results of the cohesive zone model for the solid propellant mixed-mode fracture are presented.

## **2. Experiments on the mixed-mode fracture of solid propellants**

We examined the use of a compact-tension-shear specimen to investigate the mixed mode fracture criteria for solid propellants. This specimen, shown in Fig. 1 along with the loading grips, was introduced by Buchholz *et al* (1987) and has been successfully in our laboratory in the past in examining mixed mode fracture in polymers (Mahajan and Ravi-Chandar, (1989)) and polymer interface cracks (Foltyn and Ravi-Chandar, (1990)). The stress intensity factors  $K_I$  and  $K_{II}$  for this geometry are given as (see Buchholz *et al* (1987)):



$$\begin{aligned}
\frac{K_I}{\frac{P}{wt}\sqrt{\pi a}} &= \frac{\cos \alpha}{1 - \frac{a}{w}} \sqrt{\frac{0.26 + 2.65\left(\frac{a}{w-a}\right)}{1 + 0.55\left(\frac{a}{w-a}\right) - 0.08\left(\frac{a}{w-a}\right)^2}} \\
\frac{K_{II}}{\frac{P}{wt}\sqrt{\pi a}} &= \frac{\sin \alpha}{1 - \frac{a}{w}} \sqrt{\frac{-0.23 + 1.40\left(\frac{a}{w-a}\right)}{1 - 0.67\left(\frac{a}{w-a}\right) + 2.08\left(\frac{a}{w-a}\right)^2}}
\end{aligned} \tag{4}$$

where  $\alpha$  is the angle between the normal to the crack and the load line,  $P$  is the applied load,  $a$  is the crack length,  $w$  is the specimen width and  $t$  is the specimen thickness. In the tests performed for this report, these dimensions were:  $a = 2$  in;  $w = 4$  in and  $t = 0.2$  in. The crack was introduced into the specimen by cutting a slit to half the width of the specimen. The specimen and loading attachments were placed on a specially designed test frame capable of cross head rates of up to 100 in/min; the crack tip region was captured using a videocamera in order to determine the onset of crack growth. The load and load-point-displacement were recorded from the test machine.

The experiments on the solid propellant specimens provided by the Phillips Laboratory were performed under constant rates of cross-head extension; in the range from 0.01 in/min and 10 in/min; the angle  $\alpha$  was varied in the range from 0 to 90. Three different temperatures ( $-65$  F,  $+70$  F or  $165$  F) were considered. The details of the experiments and their results are reported in the Final Report to Raytheon STX Inc, who provided the contract from Phillips Laboratory for the performance of the tests. Figs. 2, 3 and 4 summarize the results corresponding to  $+70$  F. The onset of mixed-mode crack initiation is well characterized by the MTS theory as seen in Fig. 2. There is a significant rate-dependence for the mode I stress intensity factor as shown in Fig. 3; this implies that a viscoelastic model is necessary for the characterization of the fracture of the solid propellant. Finally, in Fig. 4, the variation of the kink angle with the loading mixity is shown; clearly the MTS theory does not predict the kink direction, especially at large values of mode II loading. The large damage that is introduced near the crack tip in the process zone is believed to be the main reason for this discrepancy. In an effort to overcome this, a cohesive zone model is proposed to represent the damaged zone near the crack tip as described in the next section.

### 3. Cohesive zone model for a crack in elastostatics

In this section, we consider the idealized model of a line fracture process zone near the crack tip. This model of the fracture process zone is motivated by the fact that in some materials the crack surfaces are usually not separated completely behind the (fictitious) crack tip. There exists a relatively long extension of the crack - variously called the wake zone, the bridging zone, or cohesive zone - where tractions can be transferred across the crack line. In solid propellants, this is the damage zone in the crack tip region. The key assumption in this model is that material softening or damage accumulation beyond the peak load is localized in a narrow layer behind a fictitious crack tip, whose volume is negligible and whose action is replaceable by cohesive forces. Typically, two types of constitutive laws are used in the literature for cohesive materials: one is

characterized by a traction-displacement relationship, the other one by a material constitutive law defined in terms of stress and strain accompanied with a thickening law of the layer. In the latter, thickening of a cohesive layer is decoupled which may be worthy of studying separately in various materials considering rate-dependence and under dynamic loading. However, for quasistatic loading - the case considered predominantly in the literature - a law describing the traction-displacement relation is sufficient for modeling of the cohesive zone. We present below one such law for a cohesive crack represented by a line spring connecting two coincident crack points - this seems to be the most appropriate model for crazing-dominant brittle polymers and fiber-reinforced composites.

Consider a representation of the development of a crack shown in Fig. 5a. We suggest that two points,  $\mathbf{x}^+$  and  $\mathbf{x}^-$ , originally coincident on opposite sides of a line, separate into two distinct points, connected by the cohesive zone material; continued straining increases the separation between these two points and eventually leads to cracking. The kinematics of this separation process are assumed to be described completely by the crack face separation,  $\mathbf{w}$ . Introducing the local normal and tangent directions along the cohesive zone,  $\mathbf{w}$  can be resolved into the normal separation distance (or the cohesive zone opening displacement) component,  $w_n = u_n^- - u_n^+$  and the tangential separation distance (or the sliding displacement) component  $w_\tau = u_\tau^- - u_\tau^+$ . In order to prevent the inter-penetration of the cohesive zone,  $w_n \geq 0$ ; equality holds only in the case that there is contact between the top and bottom surfaces of the cohesive zone and in this case, we must also provide a description of the frictional resistance on the surface as well. We consider first the case of a locally opening mode crack with  $w_n > 0$  and describe the force-separation law for the cohesive zone. The cohesive material may be modeled by a simple line spring that behaves according to the following:

$$\mathbf{p} = k(w_d)\mathbf{w}, \quad (5)$$

or in component form

$$\begin{aligned} p_n &= k(w_d)w_n \\ p_\tau &= k(w_d)w_\tau \end{aligned} \quad (6)$$

where  $\mathbf{p}$  is the traction vector with normal and tangential components,  $p_n$  and  $p_\tau$ , respectively.  $w_d$  is the maximum separation distance between two originally coincident points on the crack over the entire loading history, and is used as a damage parameter. The stiffness of the cohesive zone material is denoted by  $k(w_d)$  and is assumed to depend on the current state of damage. Note that  $k(w_d)$  is a decreasing function of  $w_d$ , indicating the softening behavior of the material; this imposes an irreversibility of the damage process under unloading. Corresponding to each  $w_d$ , there exists a traction,  $p_d$ , and a damage locus derived from Eqs. (5):

$$p_d = k(w_d)w_d \quad (7)$$

The constitutive law described above is illustrated schematically in Fig. 5b. Note that the description of the cohesive zone material through the damage parameter and stiffness allows for irreversibility of damage. Upon unloading, the points on the cohesive zone unload linearly with a stiffness  $k(w_d)$ , whereas in most cohesive zone models, unloading occurs along the damage locus. Including the unloading effect has expanded the capability of the cohesive crack model in simulating realistic fracture behavior significantly. There are two critical states along the damage lo-

cus. The first one, at  $w_d = 0$  and  $p_d = p_y$ , represents the maximum traction that can be sustained by the material before the cohesive zone begins to develop; beyond this critical level, separation processes begin and  $w_d$  increases. The point on the specimen that is at this state is usually called the fictitious crack tip or the cohesive zone tip. The second critical point on the damage locus occurs at  $w_d = w_f$  and  $p_d = 0$ ; this point represents the maximum displacement jump across the cohesive zone that can be sustained before cracking; beyond this level, the traction goes to zero and the two initially coincident points are now completely separated. The point on the specimen that is at this state is usually called the physical crack tip. Hence, Eqs. (5) and (6) together, define the complete process of separation of a material point into a crack, as long as  $w_n > 0$ . A constitutive law in stress-strain for a cohesive material can be described in a similar manner (see Yang and Ravi-Chandar, 1996). The transition of that law to this law is apparent.

We now turn to the case when  $w_n = 0$ . Under arbitrary loading, contact of two crack surfaces could occur. In such cases, as shown in Fig. 6a, we must provide an appropriate description for the development of friction along the cohesive zone, in addition to the line-spring model described above. We note that this is a generic development and not particularly applicable to the case of the solid propellant; for the propellant, it might be appropriate to set the friction coefficient to zero. We model the frictional interaction simply through a Coulomb type law. Thus, the tangential interaction of the crack surfaces in contact is given by

$$p_\tau = k(w_d)w_\tau - \text{sgn}(w_\tau)fp_n, \quad (8)$$

where  $f$  is frictional coefficient. The equation for the determination of the normal component of the traction  $p_n$  is obtained by enforcing the contact condition  $w_n = 0$ . In Eq. (8), the first term represents the tangential traction contribution due to the line spring described above (nontrivially if it is not broken completely) and the second term represents the Coulomb friction component. In order to attain smooth transition of frictional force near  $w_\tau = 0$ , the frictional coefficient  $f$  may be assumed to be

$$f = \begin{cases} f_0 \frac{|w_\tau|}{w_{ad}}, & |w_\tau| \leq w_{ad}; \\ f_0, & \text{otherwise,} \end{cases} \quad (9)$$

where  $f_0$  and  $w_{ad}$  are both non-negative material constants. Function  $f$  is plotted in Fig. 6b. This completes the description of the cohesive zone material behavior.

There still remains the issue of deciding on the appropriate incorporation of this model into an elastostatic crack problem. One major question that arises is the following: *What is the criterion that can be used to grow the cohesive zone from a stress concentrator?* The incorporation of the cohesive zone model eliminates energy release criterion from consideration since the energy release rate will always be the same regardless of the direction of crack extension – it is simply the area under the damage locus, assuming a fully developed cohesive zone. The most plausible criteria, particularly for the line-spring nature of the cohesive zone mode, are stress based criteria such as the maximum principal stress criterion or the maximum tangential stress criterion at the fictitious crack tip. Assuming that one of these criteria would be appropriate, a second major question arises: *What should be the step size in extending the crack along this direction?* In finite element formulations, such as those of Xu and Needleman, (1994), and Ortiz (1996), cohesive

zones are forced to develop along element boundaries and the extension is over the side of one entire element. The approach in these models is to make the element size so small that the overall crack growth behavior is captured adequately. In other words, the macroscopic crack path is suggested to be independent of the length scale of the discretization when the latter is sufficiently small compared to characteristic structural length scale. In the present work, we choose the maximum principal stress criterion for determining the crack increment. If the maximum principal stress at a fictitious crack tip reaches the critical value,  $p_y$ , this tip is ready to run under further loading. The direction in which the tip advances is perpendicular to the direction of the maximum principal stress at that point, and the extension is such that the maximum principal stress at the new tip position is kept at the critical value  $p_y$ , during continued loading. However, note that, structural instability may occur while a crack is advancing; i.e., extension of a crack may enhance the stress state at a crack tip rather than release it. In this case, the crack may run fast and inertia effects may have to be included.

#### **4. Boundary integral formulation of the elastostatic crack problem with a cohesive zone at the crack tip**

Boundary element method (BEM) has received much attention recently, especially in application to fracture mechanics (FM) (see Cruse, 1996 and Aliabadi, 1997 for reviews). The method is attractive because it involves discretization of the boundary alone; the dimensionality of the stiffness matrix formed in BEM is then reduced by one in comparison to a domain method, such as finite element method (FEM), although the stiffness matrix is full and asymmetric in general. A particularly attractive advantage of BEM in application to crack problems over FEM is that domain remeshing is not necessary when a crack grows; only one more element of a crack is added with all the already existing elements untouched. However, as a crack is modeled mathematically with the two crack surfaces being coincident, the classic boundary integral equation (BIE) can not be applied directly or the resulting stiffness matrix formed will be ill-conditioned. A great deal of effort has been expended in dealing with this difficulty; many methods - such as the crack Green's function method (Snyder and Cruse, 1975), the displacement discontinuity method (Crouch, 1976, and Wen, 1996), the subdomains method (Blandford, Ingraffea and Liggett, 1981), the dual boundary element method (DBEM) (Hong and Chen, 1988, Portela, *et al.*, 1992, and Chen and Chen, 1995), the single-domain traction boundary element method (Young, 1996), and some hybrid methods optimizing the advantages of some of the above mentioned methods (Ameen and Raghuprasad, 1994) - have been proposed. It is not our intent to review these methods here; one may see Chen and Chen (1995) for a discussion of some of these methods. Among the methods mentioned above the method of subdomains eliminates the discrepancy noted above by cutting a cracked structure into pieces of simpler topology such that BIE can be applied properly to each of domain separately. However, this formulation increases the computational effort as a result of the additional artificial boundaries that appear from the cutting process; moreover, when a crack advances, remeshing is still needed in general. Nevertheless, the idea of the method of subdomains is valuable and is adopted in the present paper to derive a mathematically rigorous and simple formulation of the *single-domain dual-boundary-integral equations* (SDDBIEs) of a cracked structure. The classic dual integral equations for a simple structure is, of course, well established in the literature. These SDDBIEs were given by Young (1996), and applied to solve a traction-free crack problem using continuous elements.

#### 4.1. Summary of the dual integral equations for a simple structure

Consider a homogeneous, isotropic, linearly elastic domain  $\Omega$  with piecewise smooth boundary  $\Gamma$  as shown in Fig. 7. A Cartesian (Lagrangian) coordinate system<sup>1</sup> is used along with standard indicial notation. The displacement components  $u_i(\mathbf{X})$ , at a point  $\mathbf{X}$ , can be represented in the following form:

$$\underline{c}_{ij}(\mathbf{X})u_j(\mathbf{X}) = \int_{\Gamma} \left\{ u_{ij}^*(\mathbf{X}, \mathbf{x})p_j(\mathbf{x}) - p_{ij}^*(\mathbf{X}, \mathbf{x}, \mathbf{n})u_j(\mathbf{x}) \right\} d\Gamma(\mathbf{x}) + \int_{\Omega} u_{ij}^*(\mathbf{X}, \mathbf{x})b_j(\mathbf{x})d\Omega(\mathbf{x}), \quad (10)$$

where  $p_j$  are traction components,  $b_j$  are body force components.  $u_{ij}^*$  and  $p_{ij}^*$  are the fundamental solutions representing the displacements and tractions respectively in the  $j^{\text{th}}$  direction at a field point  $\mathbf{x}$  due to a unit force acting in the  $i^{\text{th}}$  direction at a source point  $\mathbf{X}$ . Note that  $p_{ij}^*$  are taken along the outward normal vector,  $\mathbf{n}$ , of  $\Gamma$  at  $\mathbf{x}$  and that with the inclusion of  $\mathbf{n}$  in  $p_{ij}^*$ , the dependence of the integrals on the normal is made explicit.  $\underline{c}_{ij}$  is a coefficient matrix given by

$$\underline{c}_{ij} = \begin{cases} \delta_{ij} & \mathbf{X} \in \Omega; \\ c_{ij} & \mathbf{X} \in \Gamma; \\ 0 & \text{otherwise,} \end{cases} \quad (11)$$

where  $\delta_{ij}$  is Kronecker delta, and  $c_{ij} = \delta_{ij}/2$  if the tangential surface at  $\mathbf{X}$  is smooth; if it is not the case one may see Hartmann (1980) for the closed-form expressions of this matrix. When  $\mathbf{X} \in \Omega$ , Eqs. (1) with  $\underline{c}_{ij} = \delta_{ij}$  is called the *Somigliana identity*. One may easily prove that, if  $\mathbf{X}$  is outside  $\Omega$  and  $\Gamma$ , Eqs. (10) holds trivially with  $\underline{c}_{ij} = 0$ . The form of Eqs. (10) most useful in the boundary integral formulation arises when  $\mathbf{X} \in \Gamma$ . Applying a limiting process as  $\mathbf{X}$  approaches a boundary, the Somigliana identity leads to the boundary integral equation of displacements (BIED, or usually BIE), based on which the classic boundary element technique is developed (Brebbia, Telles and Wrobel, 1984).

Differentiating Eqs. (10) with respect to  $\mathbf{X}$  (with  $\mathbf{X} \in \Omega$ ) the strains over  $\Omega$  can be calculated. If these strains are substituted into Hooke's law, the integral equations of stresses at a source point  $\mathbf{X}$  (with  $\mathbf{X} \in \Omega$ ) are obtained. A limiting process, similar to the one used to obtain the BIE, can be applied to the resulting integral equation as  $\mathbf{X}$  approaches a boundary, leading to the boundary integral equation of stresses. These integral equations are summarized below:

$$\underline{C}_{ik}(\mathbf{X})\sigma_{kj}(\mathbf{X}) = \int_{\Gamma} \left\{ U_{ijk}^*(\mathbf{X}, \mathbf{x})p_k(\mathbf{x}) - P_{ijk}^*(\mathbf{X}, \mathbf{x}, \mathbf{n})u_k(\mathbf{x}) \right\} d\Gamma(\mathbf{x}) + \int_{\Omega} U_{ijk}^*(\mathbf{X}, \mathbf{x})b_k(\mathbf{x})d\Omega(\mathbf{x}), \quad (12)$$

where  $U_{ijk}^*$  and  $P_{ijk}^*$  are linear combinations of derivatives of  $u_{ij}^*$  and  $p_{ij}^*$ , with respect to  $\mathbf{X}$ . As in the case of  $p_{ij}^*$ ,  $P_{ijk}^*$  are taken along the outward normal vector,  $\mathbf{n}$ , of  $\Gamma$  at  $\mathbf{x}$ .  $\underline{C}_{ij}$  is a coefficient matrix given by

<sup>1</sup> Standard index notation is used. The range for Latin subscript indices is 3 and the range for Greek subscript indices is 2. Summation over repeated subscripts over their range is implied unless suspended explicitly. Superscripts do not follow this range and summation convention; their range would be indicated explicitly and summation is indicated by the summation symbol.

$$\underline{C}_{ij} = \begin{cases} \delta_{ij} & \mathbf{X} \in \Omega; \\ \delta_{ij} / 2 & \mathbf{X} \in \Gamma; \\ 0 & \text{otherwise,} \end{cases} \quad (13)$$

which is identical to  $\underline{c}_{ij}$  provided that corner points where tractions are not well defined are excluded. If Eqs. (12) are multiplied on both sides by the outward normal vector at  $\mathbf{X}$  as  $\mathbf{X} \in \Gamma$ , then, the boundary integral equations of tractions (BIET) are obtained, which may be employed to formulate a boundary element method in a similar way as BIE.

The fundamental solutions used in the above formulation are due to Kelvin (Love, 1944), and are the basic singular solutions to a point load in an infinite medium. The components  $u_{ij}^*$  and  $p_{ij}^*$  are given below for two (plane-strain) and three dimensional problems:

$$u_{ij}^*(\mathbf{X}, \mathbf{x}) = \frac{1}{16\pi\mu(1-\nu)r} \left[ (3-4\nu)\delta_{ij} + r_{,i}r_{,j} \right], \quad (3\text{-D}) \quad (14)$$

$$u_{ij}^*(\mathbf{X}, \mathbf{x}) = \frac{1}{8\pi\mu(1-\nu)} \left[ (3-4\nu) \ln\left(\frac{1}{r}\right) \delta_{ij} + r_{,i}r_{,j} \right], \quad (2\text{-D; plane-strain}) \quad (15)$$

$$p_{ij}^*(\mathbf{X}, \mathbf{x}, \mathbf{n}) = \frac{-1}{4\bar{\alpha}\pi(1-\nu)r^{\bar{\alpha}}} \left[ \frac{\partial}{\partial n} \left( (1-2\nu)\delta_{ij} + \bar{\beta}r_{,i}r_{,j} \right) - (1-2\nu)(r_{,i}n_j - r_{,j}n_i) \right], \quad (16)$$

where  $\mu$  is shear modulus, and  $\nu$  is Poisson ratio;  $\bar{\alpha} = 2$ ,  $\bar{\beta} = 3$  for three dimensional problems and  $\bar{\alpha} = 1$ ,  $\bar{\beta} = 2$  for two-dimensional plane-strain problems. Moreover,  $r = r(\mathbf{X}, \mathbf{x})$  represents the distance between the points  $\mathbf{X}$  and  $\mathbf{x}$ , and its derivatives are taken with respect to  $\mathbf{x}$ .  $U_{ijk}^*$  and  $P_{ijk}^*$  are given by

$$U_{ijk}^*(\mathbf{X}, \mathbf{x}) = \frac{1}{4\bar{\alpha}\pi(1-\nu)r^{\bar{\alpha}}} \left[ (1-2\nu)(r_{,j}\delta_{ik} + r_{,i}\delta_{jk} - r_{,k}\delta_{ij}) + \bar{\beta}r_{,i}r_{,j}r_{,k} \right], \quad (17)$$

$$P_{ijk}^*(\mathbf{X}, \mathbf{x}, \mathbf{n}) = \frac{\mu}{2\bar{\alpha}\pi(1-\nu)r^{\bar{\beta}}} \left\{ \bar{\beta} \frac{\partial}{\partial n} \left[ (1-2\nu)r_{,k}\delta_{ij} + \nu(r_{,i}\delta_{jk} + r_{,j}\delta_{ik}) - \bar{\gamma}r_{,i}r_{,j}r_{,k} \right] \right. \\ \left. + \bar{\beta}\nu(r_{,i}n_jr_{,k} + n_i r_{,j}r_{,k}) + (1-2\nu)(\bar{\beta}n_k r_{,i}r_{,j} + n_j\delta_{ik} + n_i\delta_{jk}) - (1-4\nu)n_k\delta_{ij} \right\}, \quad (18)$$

where  $\bar{\alpha}$  and  $\bar{\beta}$  are as given above, and  $\bar{\gamma} = 5$  for three dimensional problems and  $\bar{\gamma} = 4$  for two dimensional problems. The plane strain expressions are valid for plane stress provided that  $\nu$  is replaced by  $\bar{\nu} = \nu/(1+\nu)$ . As a source point  $\mathbf{X}$  and a field point  $\mathbf{x}$  coincide on a boundary, the integral kernels of  $u_{ij}^*$ ,  $p_{ij}^*$ ,  $U_{ijk}^*$ , and  $P_{ijk}^*$  may be singular and even hypersingular. The corresponding integrals in Eqs. (10) and (12) are taken in the sense of Cauchy principal value if singular, and are taken in the sense of Hadamard principal value if hypersingular.

#### 4.2. Single-domain dual integral equations for a cracked structure

A structure containing a mathematically sharp crack degenerates the boundary integral formulation due to coincidence of the two crack surfaces. In that case, one cannot apply either BIED or

BIET to produce a boundary element method directly in general. This problem has been addressed in a number of ways: partitioning the domain into multi-domains, using crack Green's functions, the displacement discontinuity technique, and so on. In this section, we describe the formulation of a single-domain dual-boundary-integral method using Kelvin's solutions. We cut a cracked elastostatic structure into subdomains of simple topology so that the dual integral equations for a simple structure can be applied to each domain appropriately. In a further step, using the continuity and equilibrium conditions along artificial boundaries, as well as some properties of the integral kernels, we eliminate entirely the integrals involving any artificial boundaries. In order to illustrate the derivation of the single-domain integral equations, we shall consider a structure containing one crack; however, the same approach can be applied to any number of cracks in the structure. Furthermore, for simplicity, we shall ignore the body forces; if necessary, they may be added back into the final equations without any difficulty.

As shown in Fig. 8, a structure containing one crack is cut into two subdomains with a path that passes through the crack. We denote the two subdomains without a crack by  $\Omega_I$  and  $\Omega_{II}$  respectively. Their boundaries are denoted by  $\Gamma_I$  and  $\Gamma_{II}$  respectively. The topology of the subdomains is simple such that Eqs. (10) and (12) may be applied to them. This results in the following sets of equations for the displacement and traction components in the two subdomains. For the domain  $\Omega_I$ , we have

$$\underline{c}_{ij}^I(\mathbf{X})u_j^I(\mathbf{X}) = \int_{\Gamma_I} \left\{ u_{ij}^*(\mathbf{X}, \mathbf{x})p_j^I(\mathbf{x}) - p_{ij}^*(\mathbf{X}, \mathbf{x}, \mathbf{n}^I)u_j^I(\mathbf{x}) \right\} d\Gamma(\mathbf{x}), \quad (19)$$

with

$$\underline{c}_{ij}^I = \begin{cases} \delta_{ij} & \mathbf{X} \in \Omega_I; \\ c_{ij}^I & \mathbf{X} \in \Gamma_I; \\ 0 & \text{otherwise,} \end{cases} \quad (20)$$

and

$$\underline{C}_{ik}^I(\mathbf{X})\sigma_{kj}^I(\mathbf{X}) = \int_{\Gamma_I} \left\{ U_{ijk}^*(\mathbf{X}, \mathbf{x})p_k^I(\mathbf{x}) - P_{ijk}^*(\mathbf{X}, \mathbf{x}, \mathbf{n}^I)u_k^I(\mathbf{x}) \right\} d\Gamma(\mathbf{x}), \quad (21)$$

with

$$\underline{C}_{ik}^I = \begin{cases} \delta_{ik} & \mathbf{X} \in \Omega_I; \\ \delta_{ik} / 2 & \mathbf{X} \in \Gamma_I; \\ 0 & \text{otherwise.} \end{cases} \quad (22)$$

For the domain  $\Omega_{II}$ , we also have

$$\underline{c}_{ij}^{II}(\mathbf{X})u_j^{II}(\mathbf{X}) = \int_{\Gamma_{II}} \left\{ u_{ij}^*(\mathbf{X}, \mathbf{x})p_j^{II}(\mathbf{x}) - p_{ij}^*(\mathbf{X}, \mathbf{x}, \mathbf{n}^{II})u_j^{II}(\mathbf{x}) \right\} d\Gamma(\mathbf{x}), \quad (23)$$

with

$$\underline{c}_{ij}^{\text{II}} = \begin{cases} \delta_{ij} & \mathbf{X} \in \Omega_{\text{II}}; \\ c_{ij}^{\text{II}} & \mathbf{X} \in \Gamma_{\text{II}}; \\ 0 & \text{otherwise,} \end{cases} \quad (24)$$

and

$$\underline{C}_{ik}^{\text{II}}(\mathbf{X})\sigma_{kj}^{\text{II}}(\mathbf{X}) = \int_{\Gamma_{\text{II}}} \left\{ U_{ijk}^*(\mathbf{X}, \mathbf{x}) p_k^{\text{II}}(\mathbf{x}) - P_{ijk}^*(\mathbf{X}, \mathbf{x}, \mathbf{n}^{\text{II}}) u_k^{\text{II}}(\mathbf{x}) \right\} d\Gamma(\mathbf{x}), \quad (25)$$

with

$$\underline{C}_{ik}^{\text{II}} = \begin{cases} \delta_{ik}, & \mathbf{X} \in \Omega_{\text{II}}; \\ \delta_{ik} / 2, & \mathbf{X} \in \Gamma_{\text{II}}; \\ 0, & \text{otherwise.} \end{cases} \quad (26)$$

All of the functions are defined for all  $\mathbf{X}$  and are single-valued. Thus, we add Eqs. (19) and (23), and Eqs. (21) and (25) algebraically, and rearrange them in the following forms:

$$\begin{aligned} \underline{c}_{ij}^{\text{I}}(\mathbf{X})u_j^{\text{I}}(\mathbf{X}) + \underline{c}_{ij}^{\text{II}}(\mathbf{X})u_j^{\text{II}}(\mathbf{X}) = & \int_{\Gamma^{\text{ex}}} \left\{ u_{ij}^*(\mathbf{X}, \mathbf{x}) p_j(\mathbf{x}) - p_{ij}^*(\mathbf{X}, \mathbf{x}, \mathbf{n}) u_j(\mathbf{x}) \right\} d\Gamma(\mathbf{x}) + \\ & \int_{\Gamma^{c+a}} \left\{ u_{ij}^*(\mathbf{X}, \mathbf{x}) [p_j^{\text{I}}(\mathbf{x}) + p_j^{\text{II}}(\mathbf{x})] - [p_{ij}^*(\mathbf{X}, \mathbf{x}, \mathbf{n}^{\text{I}}) u_j^{\text{I}}(\mathbf{x}) + p_{ij}^*(\mathbf{X}, \mathbf{x}, \mathbf{n}^{\text{II}}) u_j^{\text{II}}(\mathbf{x})] \right\} d\Gamma(\mathbf{x}), \end{aligned} \quad (27)$$

and

$$\begin{aligned} \underline{C}_{ik}^{\text{I}}(\mathbf{X})\sigma_{kj}^{\text{I}}(\mathbf{X}) + \underline{C}_{ik}^{\text{II}}(\mathbf{X})\sigma_{kj}^{\text{II}}(\mathbf{X}) = & \int_{\Gamma^{\text{ex}}} \left\{ U_{ijk}^*(\mathbf{X}, \mathbf{x}) p_k(\mathbf{x}) - P_{ijk}^*(\mathbf{X}, \mathbf{x}, \mathbf{n}) u_k(\mathbf{x}) \right\} d\Gamma(\mathbf{x}) + \\ & \int_{\Gamma^{c+a}} \left\{ U_{ijk}^*(\mathbf{X}, \mathbf{x}) [p_k^{\text{I}}(\mathbf{x}) + p_k^{\text{II}}(\mathbf{x})] - [P_{ijk}^*(\mathbf{X}, \mathbf{x}, \mathbf{n}^{\text{I}}) u_k^{\text{I}}(\mathbf{x}) + P_{ijk}^*(\mathbf{X}, \mathbf{x}, \mathbf{n}^{\text{II}}) u_k^{\text{II}}(\mathbf{x})] \right\} d\Gamma(\mathbf{x}), \end{aligned} \quad (28)$$

where the superscript *ex* denotes an external regular boundary, the superscript *c* denotes a crack boundary, and the superscript *a* denotes an artificial boundary generated by the cutting process. Moreover, the integrals over  $\Gamma_1^{\text{ex}}$  and  $\Gamma_{\text{II}}^{\text{ex}}$  have been put together with  $\Gamma^{\text{ex}} = \Gamma_1^{\text{ex}} + \Gamma_{\text{II}}^{\text{ex}}$ ; the superscripts I and II have been dropped since  $\Gamma_1^{\text{ex}}$  and  $\Gamma_{\text{II}}^{\text{ex}}$  do not overlap. Equilibrium of the whole structure indicates that the tractions on two coincident opposite artificial boundaries are equal in magnitude and opposite in direction; *i.e.*,

$$p_i^{\text{I}}(\mathbf{x}) = -p_i^{\text{II}}(\mathbf{x}), \text{ as } \mathbf{x} \in \Gamma^a. \quad (29)$$

Also, due to the requirement of continuity of the displacement components at the coincident points on the artificial boundaries, it holds that

$$u_i^{\text{I}}(\mathbf{x}) = u_i^{\text{II}}(\mathbf{x}), \text{ as } \mathbf{x} \in \Gamma^a. \quad (30)$$

Moreover, the integral kernels in Eqs. (7) and (9) have the following properties:

$$p_{ij}^*(\mathbf{X}, \mathbf{x}, -\mathbf{n}) = -p_{ij}^*(\mathbf{X}, \mathbf{x}, \mathbf{n}), \text{ i.e., } p_{ij}^*(\mathbf{X}, \mathbf{x}, \mathbf{n}^{\text{I}}) = -p_{ij}^*(\mathbf{X}, \mathbf{x}, \mathbf{n}^{\text{II}}) \text{ as } \mathbf{x} \in \Gamma^{c+a}, \quad (31)$$

$$P_{ijk}^*(\mathbf{X}, \mathbf{x}, -\mathbf{n}) = -P_{ijk}^*(\mathbf{X}, \mathbf{x}, \mathbf{n}), \text{ i.e., } P_{ijk}^*(\mathbf{X}, \mathbf{x}, \mathbf{n}^{\text{I}}) = -P_{ijk}^*(\mathbf{X}, \mathbf{x}, \mathbf{n}^{\text{II}}) \text{ as } \mathbf{x} \in \Gamma^{c+a}. \quad (32)$$



In deriving the above, the reversal of the outward normal  $\mathbf{n}$  at the two coincident points on the crack and artificial boundaries has been applied:

$$\mathbf{n}^I(\mathbf{x}) = -\mathbf{n}^{II}(\mathbf{x}) \text{ as } \mathbf{x} \in \Gamma^{c+a}. \quad (33)$$

Using Eqs. (15), (17), and (20) through (23) to Eqs. (18) and (19), we obtain

$$\begin{aligned} I_i(\mathbf{X}) = & \int_{\Gamma^{ex}} \left\{ u_{ij}^*(\mathbf{X}, \mathbf{x}) p_j(\mathbf{x}) - p_{ij}^*(\mathbf{X}, \mathbf{x}, \mathbf{n}) u_j(\mathbf{x}) \right\} d\Gamma(\mathbf{x}) \\ & + \int_{\Gamma^c} \left\{ u_{ij}^*(\mathbf{X}, \mathbf{x}) (p_j^+(\mathbf{x}) + p_j^-(\mathbf{x})) - p_{ij}^*(\mathbf{X}, \mathbf{x}, \mathbf{n}^+) (u_j^+(\mathbf{x}) - u_j^-(\mathbf{x})) \right\} d\Gamma(\mathbf{x}), \end{aligned} \quad (34)$$

with

$$I_i(\mathbf{X}) = \begin{cases} u_i(\mathbf{X}) & \mathbf{X} \in \Omega; \\ c_{ij}(\mathbf{X}) u_j(\mathbf{X}) & \mathbf{X} \in \Gamma^{ex}; \\ c_{ij}^+(\mathbf{X}) u_j^+(\mathbf{X}) + c_{ij}^-(\mathbf{X}) u_j^-(\mathbf{X}) & \mathbf{X} \in \Gamma^c; \\ 0 & \text{otherwise,} \end{cases} \quad (35)$$

and

$$\begin{aligned} J_{ij}(\mathbf{X}) = & \int_{\Gamma^{ex}} \left\{ U_{ijk}^*(\mathbf{X}, \mathbf{x}) p_k(\mathbf{x}) - P_{ijk}^*(\mathbf{X}, \mathbf{x}, \mathbf{n}) u_k(\mathbf{x}) \right\} d\Gamma(\mathbf{x}) \\ & + \int_{\Gamma^c} \left\{ U_{ijk}^*(\mathbf{X}, \mathbf{x}) (p_k^+(\mathbf{x}) + p_k^-(\mathbf{x})) - P_{ijk}^*(\mathbf{X}, \mathbf{x}, \mathbf{n}^+) (u_k^+(\mathbf{x}) - u_k^-(\mathbf{x})) \right\} d\Gamma(\mathbf{x}), \end{aligned} \quad (36)$$

with

$$J_{ij}(\mathbf{X}) = \begin{cases} \sigma_{ij}(\mathbf{X}) & \mathbf{X} \in \Omega; \\ \sigma_{ij}(\mathbf{X}) / 2 & \mathbf{X} \in \Gamma^{ex}; \\ (\sigma_{ij}^+(\mathbf{X}) + \sigma_{ij}^-(\mathbf{X})) / 2 & \mathbf{X} \in \Gamma^c; \\ 0 & \text{otherwise,} \end{cases} \quad (37)$$

where the superscript  $+$  indicates one side of a crack, and the superscript  $-$  indicates the corresponding opposite side, instead of the superscripts I and II. The positive side of a crack may be chosen arbitrarily, for convenience. Eqs. (34) and (36) are so-called the *single-domain dual integral equations of a cracked structure*; in these equations the integrals are taken only along the regular external boundary and one side of a crack. The artificial boundaries that appeared due to the cutting process have been entirely eliminated from consideration. If a structure contains multiple cracks, the single-domain dual integral equations are given in the same forms as Eqs. (34) and (36).

Eqs. (34) and (36) with a source point on the boundary, *i.e.*,  $\mathbf{X} \in \Gamma^{ex+c}$ , are of the most importance, in the formulation of boundary integral equations for elastostatic problems. In formulating a general boundary integral method using Eqs. (36), it is advantageous to use tractions instead of stresses since the number of unknowns can be reduced. If Eqs. (36) are "multiplied" on both sides by the outward normal at the boundary point  $\mathbf{X}$  as usual the traction version of Eqs. (36) with  $\mathbf{X} \in \Gamma^{ex+c}$  can be obtained as

$$\begin{aligned}
J_{ij}(\mathbf{X})n_j(\mathbf{X}) &= \int_{\Gamma^{ex}} \left\{ U_{ijk}^*(\mathbf{X}, \mathbf{x})p_k(\mathbf{x}) - P_{ijk}^*(\mathbf{X}, \mathbf{x}, \mathbf{n})u_k(\mathbf{x}) \right\} n_j(\mathbf{X}) d\Gamma(\mathbf{x}) \\
&+ \int_{\Gamma^c} \left\{ U_{ijk}^*(\mathbf{X}, \mathbf{x})(p_k^+(\mathbf{x}) + p_k^-(\mathbf{x})) - P_{ijk}^*(\mathbf{X}, \mathbf{x}, \mathbf{n}^+)(u_k^+(\mathbf{x}) - u_k^-(\mathbf{x})) \right\} n_j(\mathbf{X}) d\Gamma(\mathbf{x}). \quad (38)
\end{aligned}$$

Note that, as  $\mathbf{X} \in \Gamma^c$ ,  $n_j(\mathbf{X})$  is taken to be the outward normal of the positive crack side, i.e.,  $n_j(\mathbf{X}) = n_j^+(\mathbf{X})$ .

Note that on the crack surfaces, the tractions are self-equilibrating and hence

$$n_j^+(\mathbf{X})(\sigma_{ij}^+(\mathbf{X}) + \sigma_{ij}^-(\mathbf{X}))/2 = p_i^+(\mathbf{X}) \text{ and } p_i^+(\mathbf{x}) + p_i^-(\mathbf{x}) = 0. \quad (39)$$

Eqs. (39) can be used to simplify Eqs. (34), (36) and (38) when applying to cracks. In this case, traction and displacement jump on a crack may be regarded as independent variables in a numerical formulation, with the least unknowns.

#### 4.3. Iterative boundary element method of successive over-relaxation

The behavior of the cohesive zone materials and the criterion for crack advance described in the last section require that an incremental loading procedure be used when solving boundary value problems. Moreover, an iteration process is indispensable in each loading step in general due to the fact that the constitutive law of the cohesive zone material, given in Eqs. (5) - (9), involves irreversible damaging process, and is essentially history-dependent. Furthermore, the stiffness of the model line spring of the cohesive zone material,  $k(w_d)$ , is in general a part of the solution, which may or may not be dependent on the current displacement discontinuity; in other words, there is no simple relationship between the traction and displacement discontinuity on a crack which may be used to achieve a linear system of equations to solve the problems numerically. Two strategies of iteration are possible in general: in the first, a linear system of equations of the discretized problem is formulated using the stiffness of the cohesive zone material obtained in the previous iteration step, and is solved by a typical solver either direct or iterative. The stiffness of the cohesive zone material is then modified based on this solution, and the process is repeated until the solution of the desired accuracy is achieved. In the second strategy, a nonlinear system of equations of the discretized problem is formulated using the stiffness of the cohesive zone material as unknowns, and is solved iteratively. By the first strategy, the iterative procedure is very clear and the convergence of the iteration process is expected. However, it is apparently time-consuming even with a very efficient solver of a linear system of equations; the linear system of equations is solved fully many times until a solution is achieved. On the other hand, the total time for a solution by the second strategy, if a good iterative procedure is found, would be in the same order as that for one step of the iteration by the first strategy (solving the linear system of equations once). In the present work, we adopt the second strategy and formulate an iterative method of successive over-relaxation for the present nonlinear problem of a cohesive crack. The solution procedure of this iterative method will be described below, following discretization of the boundaries and the boundary integral equations.

The boundaries of a cracked two-dimensional structure are approximated by straight elements,  $\Gamma_{el}$ s, of which each contains  $N_{el}$  nodes that are uniformly distributed in it, as shown in Fig. 9. These nodes are numbered separately on the external boundary and on the crack locus. Assume that we have  $N^{ex}$  nodes on the external boundary and  $N^c$  nodes on the crack locus. A field quan-

tity,  $\mathbf{q}(\mathbf{x})$  can be approximated over an element  $\Gamma_{el}$  by interpolating the nodal values,  $\mathbf{q}^n$  in this element as

$$\mathbf{q}(\mathbf{x}) = \sum_{n=1}^{N_{el}} \phi^n(\mathbf{x}) \mathbf{q}^n, \quad (40)$$

where the interpolation function,  $\phi^n(\mathbf{x})$  satisfies the following conditions:

$$\phi^n(\mathbf{x}^m) = \begin{cases} 1 & m = n; \\ 0 & m \neq n, \end{cases} \text{ and } \sum_{n=1}^{N_{el}} \phi^n(\mathbf{x}) = \begin{cases} 1 & \mathbf{x} \in \Gamma_{el}; \\ 0 & \mathbf{x} \notin \Gamma_{el}. \end{cases} \quad (41)$$

The interpolation functions may be constant, linear or quadratic, depending on the required accuracy of the representation. Substitute Eq. (40) into Eqs. (34) and (38) with  $\mathbf{X} \in \Gamma^{ex+c}$ , the discretized forms of the dual boundary integral equations are obtained. Thus, one obtains

$$\sum_{n=1}^{N^{ex}} (g_{\alpha\beta}^{mn} p_{\beta}^n - h_{\alpha\beta}^{mn} u_{\beta}^n) + \sum_{n=N^{ex}+1}^{N^{ex}+N^c} h_{\alpha\beta}^{mn} w_{\beta}^n - I_{\alpha}(\mathbf{X}^m) = 0, \quad m = 1, 2, \dots, N^{ex} + N^c, \quad (42)$$

and

$$\sum_{n=1}^{N^{ex}} (G_{\alpha\beta}^{mn} p_{\beta}^n - H_{\alpha\beta}^{mn} u_{\beta}^n) + \sum_{n=N^{ex}+1}^{N^{ex}+N^c} H_{\alpha\beta}^{mn} w_{\beta}^n - J_{\alpha\beta}(\mathbf{X}^m) n_{\beta}(\mathbf{X}^m) = 0, \quad m = 1, 2, \dots, N^{ex} + N^c. \quad (43)$$

Eqs. (38) and (39) each represent  $2(N^{ex} + N^c)$  equations that are the discretized version of Eqs. (25) and (29). In these equations,  $g_{\alpha\beta}^{mn}$ ,  $h_{\alpha\beta}^{mn}$ ,  $G_{\alpha\beta}^{mn}$ , and  $H_{\alpha\beta}^{mn}$  are given explicitly by:

$$g_{\alpha\beta}^{mn} = \int_{\Gamma^n} u_{\alpha\beta}^*(\mathbf{X}^m, \mathbf{x}) \phi^n(\mathbf{x}) d\Gamma(\mathbf{x}), \quad (44)$$

$$h_{\alpha\beta}^{mn} = \int_{\Gamma^n} p_{\alpha\beta}^*(\mathbf{X}^m, \mathbf{x}, \mathbf{n}) \phi^n(\mathbf{x}) d\Gamma(\mathbf{x}), \quad (45)$$

$$G_{\alpha\beta}^{mn} = \int_{\Gamma^n} U_{\alpha\delta\beta}^*(\mathbf{X}^m, \mathbf{x}) \phi^n(\mathbf{x}) n_{\delta}(\mathbf{X}^m) d\Gamma(\mathbf{x}), \quad (46)$$

$$H_{\alpha\beta}^{mn} = \int_{\Gamma^n} P_{\alpha\delta\beta}^*(\mathbf{X}^m, \mathbf{x}, \mathbf{n}) \phi^n(\mathbf{x}) n_{\delta}(\mathbf{X}^m) d\Gamma(\mathbf{x}), \quad (47)$$

where  $\Gamma^n$  is the element where the  $n^{\text{th}}$  node is located. Eqs. (44) through (47) may be evaluated numerically if  $\mathbf{X}^m \notin \Gamma^n$ , and analytically if  $\mathbf{X}^m \in \Gamma^n$ . Note that the condition for a self-equilibrating crack, Eq. (39), has been used in the above equations. If  $\mathbf{u}$  and  $\mathbf{p}$ , are a trial set of displacements and tractions, Eqs. (42) and (43) would not be satisfied in general; instead, we obtain the following residuals:

$$r_{\alpha}^m(\mathbf{u}, \mathbf{p}) = \sum_{n=1}^{N^{ex}} (g_{\alpha\beta}^{mn} p_{\beta}^n - h_{\alpha\beta}^{mn} u_{\beta}^n) + \sum_{n=N^{ex}+1}^{N^{ex}+N^c} h_{\alpha\beta}^{mn} w_{\beta}^n - I_{\alpha}(\mathbf{X}^m), \quad m = 1, 2, \dots, N^{ex} + N^c, \quad (48)$$

$$R_{\alpha}^m(\mathbf{u}, \mathbf{p}) = \sum_{n=1}^{N^{ex}} (G_{\alpha\beta}^{mn} p_{\beta}^n - H_{\alpha\beta}^{mn} u_{\beta}^n) + \sum_{n=N^{ex}+1}^{N^{ex}+N^c} H_{\alpha\beta}^{mn} w_{\beta}^n - J_{\alpha\beta}(\mathbf{X}^m) n_{\beta}(\mathbf{X}^m), \quad m = 1, 2, \dots, N^{ex} + N^c.$$

(49)

We call  $r_\alpha^m$  the displacement residual and  $R_\alpha^m$  the traction residual. If the residuals are close enough to zero, the trial set of  $\mathbf{u}$  and  $\mathbf{p}$  represents an approximate solution of the boundary value problem. At all regular boundary points, either the displacement or the traction vector components are prescribed; thus only one of Eqs. (48) and (49) would be used in assembling the overall system of equations. For points that are in the cohesive zone, both the traction vector and the displacement discontinuity vector are unknown but related to each other through the constitutive description of the cohesive zone material provided in Eqs. (5) - (9). From Eq. (49), for a point  $m$  that lies on the cohesive zone, the residual can be written as a relation between the displacement jump vector  $\mathbf{w}(\mathbf{X}^m)$  and the traction vector  $\mathbf{p}(\mathbf{X}^m)$ . Note that points on the crack are simply special cases of the cohesive zone where the stiffness has decreased to zero and where  $\mathbf{w}(\mathbf{X}^m)$  is unrestricted except that  $w_n(\mathbf{X}^m) \geq 0$ . Hence the complete set of all residuals at all nodal points can be calculated. Note that in order to incorporate the crack opening, crack sliding, and crack contact modes of deformation in a convenient way, field quantities in the discretized equations must be transformed into the local orthogonal coordinates in terms of the normal and tangential directions. We now turn to a description of an iterative solution scheme for solving Eqs. (48) and (49) for  $\mathbf{u}$  and  $\mathbf{p}$ .

For a node  $m$  on the external boundary, either Eq. (48) or Eq. (49) could be used, depending on whether the imposed boundary condition at that point is a displacement or a traction condition. For the iterative solution scheme, in general, a field quantity  $q_\alpha^{m,l+1}$  at the  $(l+1)^{\text{th}}$  iteration is written in terms of its value at the  $l^{\text{th}}$  iteration,  $q_\alpha^{m,l}$ , and an increment that depends on the residuals as

$$q_\alpha^{m,l+1} = q_\alpha^{m,l} - \frac{\bar{R}}{\partial \bar{R} / \partial q_\alpha^m} \Big| \quad (50)$$

where  $\bar{R}$  is the appropriate residual for the field quantity  $q_\alpha^m$  at the  $l^{\text{th}}$  iteration. At the  $(l+1)^{\text{th}}$  iteration step, the displacement component at this node,  $u_\alpha^{m,l+1}$ , if not prescribed as a boundary condition, is calculated using the results at the  $l^{\text{th}}$  iteration by

$$u_\alpha^{m,l+1} = u_\alpha^{m,l} + \omega r_\alpha^m(\mathbf{u}, \mathbf{p}) / (C_{\alpha\alpha} + h_{\alpha\alpha}^{mm}), \quad (\text{no sum on } \alpha) \quad (51)$$

where  $\omega$  is an adjustable factor of relaxation. The displacement residual,  $r_\alpha^m(\mathbf{u}, \mathbf{p})$ , is computed using the nodal values at the  $(l+1)^{\text{th}}$  iteration step if available, or at the  $l^{\text{th}}$  iteration step. Similarly, a traction component,  $p_\alpha^{m,l+1}$ , if not prescribed as a boundary condition, is calculated using the results at the  $l^{\text{th}}$  iteration by

$$p_\alpha^{m,l+1} = p_\alpha^{m,l} + \omega R_\alpha^m(\mathbf{u}, \mathbf{p}) / (0.5 - G_{\alpha\alpha}^{mm}), \quad (\text{no sum on } \alpha) \quad (52)$$

where the traction residual,  $R_\alpha^m(\mathbf{u}, \mathbf{p})$ , is dealt with in the same way as  $r_\alpha^m(\mathbf{u}, \mathbf{p})$ . For a node  $m$  which is on the cohesive zone, we calculate the displacement discontinuity,  $w_\alpha^{m,l+1}$ , in opening mode by

$$w_\alpha^{m,l+1} = w_\alpha^{m,l} + \varpi R_\alpha^m(\mathbf{u}, \mathbf{p}) / (k^{m,l} - H_{\alpha\alpha}^{mm}), \quad (\text{no sum on } \alpha) \quad (53)$$

where  $\varpi$  is another adjustable factor of relaxation, and  $k^{m,l}$  is calculated using Eq. (31) with  $|\mathbf{w}^{m,l}|$ . If the normal component of  $\mathbf{w}$  at the  $(l+1)^{th}$  iteration step,  $w_n^{m,l+1}$ , is negative, it is set to be zero for no penetration of the crack surfaces. The tangential component of  $\mathbf{w}$  at the  $(l+1)^{th}$  iteration step,  $w_\tau^{m,l+1}$ , is re-calculated by

$$w_\tau^{m,l+1} = w_\tau^{m,l} + \varpi R_\tau^m(\mathbf{u}, \mathbf{p}) / (k^{m,l} - f_0 p_n^{m,l+1} / \bar{w}_{ad} - H_{\tau\tau}^{mm}), \quad (\text{no sum on } \tau) \quad (54)$$

where the frictional mode of the cohesive crack is activated.  $\bar{w}_{ad} = w_{ad}$  if  $|w_\tau^{m,l}| \leq w_{ad}$ ; otherwise  $\bar{w}_{ad} = |w_\tau^{m,l}|$ . Note that no special iterative process for mixed crack opening and contact is necessary.

We now describe the marching scheme used in the numerical solution; the solution procedure is implemented in three steps. Suppose that the solution at a previous loading step is already known. In order to solve the problem in the current loading step, first the cracked body is iterated to be in equilibrium with all the current cohesive nodes being held at the same displacement, using Eqs. (51) and (52); in this step, the cohesive zone material law is not used. In the second step, the cohesive zone nodes are made free to displace according to the constitutive laws described above. The whole body is iterated again to be in equilibrium using Eqs. (51) through (54). This holding and releasing process is found to produce quicker convergence for the iteration process than other schemes when a crack is advancing. The absolute difference of either displacement or traction at a boundary node between two next iteration steps is used to judge the convergence. The best relaxation factors of  $\omega$  and  $\varpi$  can be obtained through some trial computations and these factors vary in general with the geometrical configuration of the body and loading conditions. Note that in the second step, the fictitious crack tip has not been allowed to move. After the equilibrium of the cracked body is obtained without crack advance, in the third step, stresses at a point of the fictitious crack tip are calculated using Eq. (36); note that a constant element is always used at the fictitious crack tip avoiding the difficulty of the integration due to the hypersingularity in the fundamental solution. If the maximum principal stress at this point is over the critical value, *i.e.*  $p_y$ , the fictitious crack tip is forced to advance a small increment in the direction perpendicular to the maximum principal stress. This is accomplished by increasing the length of the last cohesive tip element if the advance step is smaller than a specific value; otherwise, a new crack element would be added. In this paper, we set the crack advance step to be equal to the cohesive zone tip element size; the ratio of the crack advance step to the crack element size could play a role in determining the local crack patterns in situations where the crack path is unstable, but this issue is not considered in this paper. Note that in general, a numerical stepwise scheme of crack advance may generate sharp corners between the approximating straight elements of a crack which may concentrate stresses; these stress concentrations are of a lower order than the crack tip concentration. Investigating the role of these corners problem is of less interest than that of examining the crack tip; thus, in the present paper, we neglect the weaker corner singular point while dealing with a crack. Note also that at the current loading level, the above procedure of crack advance is repeated, and the iterative solution over whole body is obtained until the maximum principal stress is not above  $p_y$  at any point in the body. This procedure achieves the solution in the current loading step. The load is then incremented and the procedure repeated to march both the loading and the crack extension. In the following, we shall

apply the method formulated above to some problems of a cohesive crack, and demonstrate the capacity of this method.

## 5. Applications

We turn to a demonstration of the capability of the boundary element strategy for handling of the cohesive cracks described above. In order to explore different aspects of the constitutive model for the cohesive zone that has been assumed in this paper, we consider two problems. The first problem concerns a single-edge-crack in a rectangular specimen under uniform far field tensile loading. For small initial crack lengths the crack extension in this configuration is unstable under displacement control; however, deep cracks exhibit stable crack growth. The results of this problem are discussed in Section 5.1. The second problem considered is a demonstration of the capability of the formulation to handle mixed-mode crack growth and crack interaction; using the same loading as in the first problem, but with an offset double-edge crack configuration, the trajectories of the two edge cracks are tracked. The results described in Section 5.2 show that the model duplicates the commonly observed behavior of two approaching cracks, and that the crack patterns exhibit a sort of bifurcation with the offset.

The following conditions describe the details of the simulation that are common to both problems. The domain of interest is a rectangular two-dimensional region of length  $l$  and height  $h$ , taken equal to  $l$  in these simulations. In these simulations, all length quantities are normalized by  $l$ ; while this is not a natural length scale for the fracture problem, it is convenient and easily interpreted. If it is desired, a scaling to an intrinsic length scale, such as the critical crack opening displacement for the cohesive zone,  $w_f$ , may be effected easily. The deformation of the specimen is assumed to be in plane-strain. An initial process zone of length 0.02 is assumed to exist at the tip of all cracks in all simulations described in this paper; the damage parameter  $w_d$  is assumed to increase linearly from zero at the fictitious crack tip to  $w_f$  at the physical crack tip. Note that this initial damage zone can be prescribed arbitrarily and is in general unknown in the physical problem. The boundaries are discretized into discontinuous elements with a constant or quadratic interpolation over the element. Specifically, the straight-line segments on the external boundary are divided into 10 elements with quadratic interpolation; the length of each element is 0.1 and the nodal spacing is 0.0333. The initial crack (outside of the cohesive zone) is also divided into quadratic elements with a nodal spacing 0.01. The initial process zone is divided into equally-spaced elements of size 0.01 with quadratic interpolation, except for the element at the fictitious crack tip which is taken to be a constant element. When a fictitious crack tip advances, one new constant element of size 0.01 is added as the corresponding new fictitious crack tip element. The old fictitious crack tip element that is now an interior element within the cohesive zone is then redefined as a quadratic element using three nodes inside it. The constitutive law of the cohesive crack is assumed to be represented by a straight line as shown in Fig. 10, which is certainly the simplest one defined by the two parameters  $p_y$  and  $w_f$ ; these parameters are taken to be  $p_y = 0.01$  and  $w_f = 0.001$ . Note that all stress and traction quantities are normalized by  $\mu l$ . Poisson's ratio is taken to be 0.3. The unloaded specimen is initially in a stress free state. It is loaded incrementally in the direction perpendicular to the top and bottom boundaries under displacement control. The increment of the loading displacement is taken to be  $1\text{E-}5$  in tension and  $-1\text{E-}4$  in compression. The relaxation factors were chosen initially by trial and error and were subsequently fixed at  $\omega = 0.6$  and  $\varpi = 1.4$ .

In the following simulations, the boundary (including the cracks) is discretized into 150 to 350 nodes depending on the crack length resulting in a system of 300 to 700 equations (or degrees of freedom). In addition there are a few equations that provide the connection between tractions and crack opening displacements on the cohesive zone. If the stiffness of the cohesive zones is not modified by damage, for each loading step, fewer than 100 iteration steps are needed to achieve a solution to the system of equation, with an accuracy of  $1\text{E-}8$  in traction components and  $1\text{E-}9$  in displacement components. If the stiffness of the cohesive zones changes through damage, but still without propagation of the fictitious crack tips, slightly more than 100 iteration steps are required for each loading step. If a new cohesive element is added and accumulates damage, each loading step requires between 150 and 400 iteration steps. If the fictitious crack tip movement is sensitive to the load, quite a few new crack elements are added in one loading step; in this case, the required iteration steps may be as large as 1000, depending on the number of the new crack elements; fortunately, this does not happen often. We ran the code for the following problems on a Digital Alpha Workstation (200 4/100). Depending on the size of the discretized system, between 10 and 30 iteration steps can be performed in one second. Run times are as short as  $\frac{1}{2}$  hours for small crack extensions; if long crack extensions are to be simulated the time required increases to the order of a few hours.

### 5.1. *Single edge crack under tension*

A number of simulations were performed with a single-edge-crack in the rectangular geometry shown in Fig. 11. The crack was considered to be along the line of symmetry and its initial length,  $a_0$ , was varied from 0.03 to 0.78. The variation of the total load on the top boundary with the imposed elongation obtained from the simulations is shown in Fig. 12. The main result, of course, is that in these simulations, simply by prescribing the applied loads and the cohesive law, initiation and growth of the crack appear naturally. These results are the mode-I analog of results that were obtained under mode III by Yang and Ravi-Chandar, (1998) using a finite difference scheme. A number of remarks regarding these simulations are listed below:

- During the loading process of a stable configuration, the fictitious crack tip starts to advance first. Note that the critical point of load at which the fictitious crack tip starts moving is of no significance since it is dependent on the initial state of the cohesive zone. With continued loading, the physical crack tip also starts to move. At this stage, the two crack tips advance at the same rate, keeping the size of the cohesive zone-defined as the distance between the fictitious and physical crack tips - a constant at about 0.1. This is considered to be the fully developed equilibrium cohesive zone size under this condition; of course, the size depends on the cohesive material model and the geometrical constraint imposed in the specimen.
- If the initial crack length,  $a_0$ , is small, crack initiation is unstable even under displacement controlled loading. In the numerical procedure, this is manifested by the fact that the stress, calculated at a point ahead of the fictitious crack tip is larger than  $p_y$ , even after the crack extension procedure has been applied over a length of many cohesive elements. This can also be inferred from the fact that the critical load for the onset of instability decreases with increasing initial crack length. Thus, crack extension and structural instability coincide in these cases. If the initial crack length is larger than about 0.48, crack extension is stable under displacement control. We examine later some issues related to crack paths in this range of stable crack growth. The behavior indicated by the sudden drop of load, for initial crack lengths less than 0.48 is usually referred to as a snap-back instability in structural mechanics. Note that the snap-back instability is also predicted by the stress intensity factor based linear elastic

fracture mechanics and is simply a structural feature of this configuration; it is not influenced qualitatively by the fracture model.

- The evolution of the crack opening profiles and the cohesive tractions at the onset of unstable crack extension are shown in Figs. 9 and 10 for a few initial crack lengths in the unstable region. Note that all these cracks had an initial cohesive zone of length 0.02 prior to load application. For long initial crack lengths, a steady-state cohesive zone of length 0.1 develops. However, for small initial crack lengths, at the onset of unstable crack extension, the cohesive zone is not completely developed. In other words, for short initial crack lengths, structural instability appears before development of a self-similar crack tip process zone. If the dissipation in the cohesive zone is computed, the result indicates that the dissipation is a function of crack length. Note that the data used for Figs. 13 and 14 were obtained based on the numerical procedure of the loading displacement increment equal to  $1E-5$ . A finer loading displacement increment may produce more developed cohesive zones representing their critical states instead of the ones plotted in Figs. 12 and 14; however, this characteristic of incomplete development of the critical process zone at the onset of unstable crack initiation will not change. A similar behavior was identified in the mode III simulation by Yang and Ravi-Chandar (1998) and used to determine the range of applicability of a single parameter characterization of fracture.

In addition to the structural stability, the stability of the crack path is also of interest in crack problems. The single-edge-notched geometry used here is very stable to perturbations in the crack path. This is demonstrated by the results of the simulations shown in Fig. 15. Here the crack paths obtained from three simulations are shown. The only difference between these simulations is that the edge crack is offset from the line of symmetry by  $d_{offset}$ . This offset, if non-zero, imposes a mixed-mode loading at the crack tip with the result that the crack path is no longer straight. The path stability of the crack is indicated by the fact that these cracks tend towards the line of symmetry. The main idea here is to demonstrate the capability of the present boundary element formulation to track arbitrary crack path evolution. Further investigations into the influence of the loading on the crack path stability are still under progress.

## 5.2. Interaction of cracks in the double edge cracked specimen

The last problem we consider in this paper is a double-edge-crack loaded in tension allowing crack interaction. This problem also provides an opportunity to examine cracks that exhibit structural instability. The geometry of the specimen is shown in Fig. 16. The initial lengths of the two edge-cracks,  $a_{1o}$  and  $a_{2o}$ , are both set equal to 0.28. Each crack tip is again provided with an initial cohesive zone of length 0.02. In order to examine the approach of the two cracks towards each other, an offset  $d_{offset}$  is provided between the two edge cracks. The load-elongation curves for two cases of  $d_{offset}$  equal to 0.1 and 0.2 respectively are shown in Fig. 17. The deformed configurations showing the crack paths determined from the simulations are presented in Figs. 18 and 19. The main observations and results are described as follows:

- Initiation of the fictitious and physical crack tips is very similar to the cases described in Section 5.1. Note that the full geometry of the specimen is modeled and the anti-symmetry of the offset cracks has not been imposed externally. For both cases, the cohesive ones at both crack tips are fully developed.
- For both simulations with  $d_{offset} = 0.1$  and 0.2, after initial stable extension of both crack tips over a length of about 0.1, structural instability occurs and the equilibrium formulation of the



problem may no longer be appropriate. At this point, the cohesive zone is fully developed. If we assume that the inertial effects are small in dictating the crack path, we may be able to determine the path evolution of these interacting cracks. We used the following strategy in our simulations to determine the crack extension behavior. At the onset of structural instability, the trajectory of the maximum principal stress from the crack tip is evaluated first; the cohesive zone - *i.e.*, the fictitious and physical crack tips - is then extended along this predetermined path, at fixed global displacement, until the stress ahead of the fictitious crack tip falls to  $p_y$  so that stability is restored. After propagating the crack according to this strategy for a length of about 0.1, stability is restored. We note, however, that this scheme did not work very well when the offset was very small indicating that inertia effects may indeed be significant and should be taken into account.

- It is interesting to note that, in Fig. 18 for  $d_{offset} = 0.1$ , the two cracks initially ‘repel each other, pass over one another (overlap) and eventually approach each other along a curved path. This is very similar to the experimental observations of Melin (1983). On the other hand, in Fig. 19 for  $d_{offset} = 0.2$ , the two crack tips ‘attract’ each other right from initiation. From a different point of view, the two crack tips approach the line of symmetry separately without much interaction in the early stages; we note that a single offset crack shows the tendency to approach the line of symmetry as demonstrated in Section 5.1. After initial extensions of the both cracks over a length of about 0.1 each, the left crack is completely shielded by the growth of the right side crack and only one crack grows in this case. The change of crack patterns with  $d_{offset}$  is a bifurcation phenomenon of significant interest (see for example, Mulhaus *et al.*, 1996). The bifurcation can be understood in the following terms: consider unequal extension of one of the crack tips due to perturbations. For cracks with small initial offset distances, perturbations in the development of either crack tip results in increased loading of the lagging crack tip while for large initial offset distances, these perturbations result in an increased loading at the leading crack tip.

## 6. Mixed-mode fracture with a cohesive zone

In order to evaluate the influence of the development of a cohesive zone near the crack tip on the mixed-mode fracture behavior, the formulation described above was used to simulate the experiments described in Section 2. The geometry is as shown in Fig. 11, with the  $d_{offset} = 0$  and the load applied at an angle  $\theta$  to the  $x_I$  axis. The results are described in Figs. 20 to 22. In Fig. 20, the variation of the load against the load-point displacement is shown. For comparison, the corresponding linear elastic fracture mechanics results are also shown. Clearly, the two results indicate a good comparison suggesting that the maximum tangential stress criterion should be a good predictor for the initiation of crack extension. Note that we have used an assumed form of the cohesive zone model and hence are not yet able to make quantitative comparisons with the experimental results. The comparison of the crack path predicted by LEFM and the cohesive zone model is shown in Fig. 21 and an enlarged view near the initial crack is shown in Figure 22. The deviation between the predictions of LEFM and the cohesive zone model in determining the crack path are clear. We believe that this is an indication that the development of damage near the crack tip leads to significant changes in the evolution of the crack path. Note that we have not provided any time dependence to the material behavior in this simulation; this will introduce further departure in the development of the crack tip process zone and hence in the crack path evolution. This aspect of mixed-mode crack growth is under further study.

## 7. Conclusions

A single-domain, dual-boundary integral formulation of elastostatic crack problems incorporating a cohesive zone model for the evolution of the fracture process is demonstrated in this paper. The cohesive zone is modeled as a damaging material with a prescribed behavior relating the applied force to the crack opening displacement. The irreversible nature of the damage is introduced through the damage parameter  $w_d$ , the maximum displacement experienced by a point on the cohesive zone during its history. The introduction of the cohesive zone necessitates an iterative solution procedure to solve the equations resulting from the boundary integral formulation; the method of successive-over-relaxation is used in this study. In terms of numerical simulations, the approach described here presents significant advantages over grid-based finite element methods since the present formulation (i) does not force development of the crack along element boundaries and thereby introduce mesh size and element geometry dependencies, (ii) does not require fine nodal spacing except within the cohesive zone, and (iii) does not require remeshing with crack extension. Three example problems were considered to demonstrate the capability of this formulation to handle arbitrary in-plane crack problems, including mixed-mode problems, contact problems, and crack interaction problems.

## 8. References

- Aliabadi, M.H. (1997), Boundary element formulations in fracture mechanics, *Applied Mechanics Reviews*, **50**, 83-96.
- Ameen, M., and Raghuprasad, B. K., (1994), A hybrid technique of modeling of cracks using displacement discontinuity and direct boundary element method, *International Journal of Fracture*, **67**, 343-355.
- Blandford, G. E., Ingrassia, A. R. and Liggett, J. A., (1981), Two-dimensional stress intensity factor computations using the boundary element method, *International Journal of Numerical Methods in Engineering*, **17**, 387-404.
- Brebbia, C. A., Telles, J. C. F. and Wrobel, L. C., (1984), **Boundary Element Techniques: Theory and Applications in Engineering**, Springer-Verlag.
- Buchholz, F.G., Pirro, P.J.M, Richard, H.A., and Dreyer, K.H., 1987, Proceedings, Fourth International Conference on Numerical Methods in Fracture Mechanics, (eds Luxmore *et al.*), Pineridge Press, Swansea, UK, p.641.
- Chen, W. H. and Chen, T. C., (1995), An efficient dual boundary element technique for a two-dimensional fracture problem with multiple cracks, *International Journal of Numerical Methods in Engineering*, **38**, 1739-1756.
- Crouch, S. L., (1976), Solution of plane elasticity problems by the displacement discontinuity method, *International Journal of Numerical Methods in Engineering*, **10**, 301-342.
- Cruse, T.A., (1996), BIE fracture mechanics analysis: 25 years of developments, *Computational Mechanics*, **18**, 1-11.
- Erdogan, F., and Sih, G.C., 1963, "On the crack extension in plates under plane loading under transverse shear", *Journal of Basic Engineering*, **85D**, pp.519-527.
- Foltyn, P., and Ravi-Chandar, K., 1991, "Initiation of an interface crack under mixed-mode loading", accepted for publication in the Journal of Applied Mechanics.

- E.C. Francis et al., 1980 "Predictive techniques for failure mechanisms in solid rocket motors", AFRPL-TR-79-87.
- Hartmann, F., (1980), Computing the C-matrix in non-smooth boundary points, in **New Developments in Boundary Element Methods** (Brebbia, C.A., Ed.), Butterworths, London, 367-379.
- Hong, H. and Chen, J., (1988), Derivations of integral equations of elasticity, *J. Engr. Mech.*, ASCE, **114**, 1028-1044.
- Love, A. E. H., (1944), **A Treatise on the Mathematical Theory of Elasticity**, Dover, New York.
- Mahajan, R.V., and Ravi-Chandar, K., 1989, "An experimental investigation of mixed-mode fracture", *International Journal of Fracture*, **41**, pp.235-252.
- Maiti, S.K., and Smith, R.A., 1983, "Comparison of the criteria for mixed-mode brittle fracture based on the preinstability stress field. Part I: Slit and elliptical cracks under uniaxial tensile loading", *International Journal of Fracture*, **23**, pp.281-295
- Melin, S., (1983), Why do cracks avoid each other? *International Journal of Fracture*, **23**, 37-45.
- Mulhaus, H.-B., Chau, K.T., and Ord, A., (1996), Bifurcation of crack pattern in arrays of two-dimensional cracks. *International Journal of Fracture*, **77**, 1-14.
- Ortiz, M., (1996), Computational micromechanics, *Computational Mechanics*, **18**, 321-338.
- Portela, A., Aliabadi, M. H. and Rooke, D. P., (1991), The dual boundary element method: effective implementation for crack problems, *International Journal of Numerical Methods in Engineering*, **33**, 1269-1287.
- Snyder, M. D. and Cruse, T. A., (1975), Boundary integral equation analysis of cracked anisotropic plates, *International Journal of Fracture*, **11**, 315-342.
- Ueda, Y. et al., 1983, "Characteristics of brittle fracture under general combined modes including those under bi-axial tensile loads", *Engineering Fracture Mechanics*, **18**, pp.1131-1158.
- Wen, P.H., (1996), Dynamic fracture mechanics: Displacement discontinuity method, Computational Mechanics Publications.
- Williams, J.G., and Ewing, P.D., 1972, "Fracture under complex stress- the angled crack problem", *International Journal of Fracture*, **8**, pp.441-446.
- Yang, B., and Ravi-Chandar, K., (1996), On the role of the process zone in dynamic fracture, *Journal of the Mechanics and Physics of Solids*, **44**, 1955-1976.
- Yang, B., and Ravi-Chandar, K., (1998), Anti-plane shear crack growth under quasistatic loading in a damaging materials, *International Journal of Solids and Structures*, in press.
- Young, A., (1996), A single-domain boundary element method for 3-d elastostatic crack analysis using continuous elements, *International Journal of Numerical Methods in Engineering*, **39**, 1265-1293.
- Xu, X.-P., and Needleman, A., (1994), Numerical simulations of fast crack growth in brittle solids, *Journal of Mechanics and Physics of Solids*, **42**, 1397-1434.

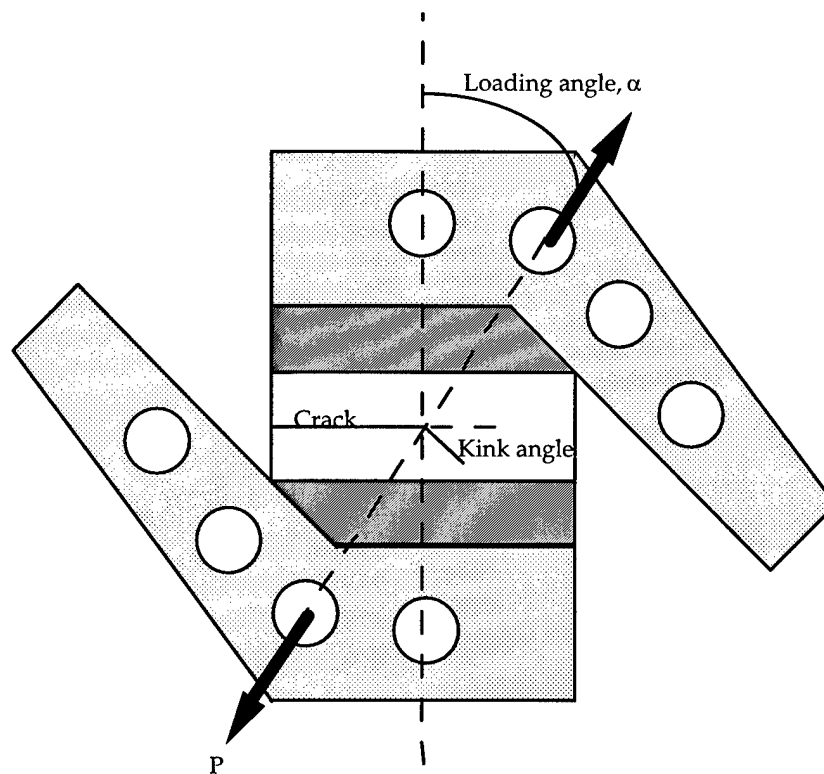


Figure 1. Mixed-mode loading geometry and grip attachments.

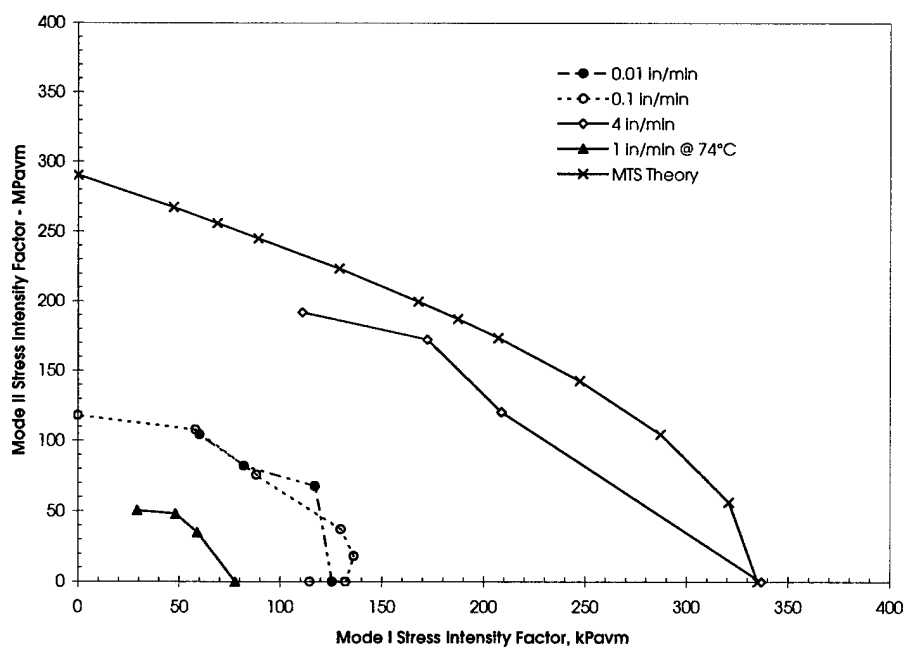


Figure 2. Failure interaction curve showing critical values of the mode-I and mode II stress intensity factors at crack initiation. The prediction of the MTS theory is also indicated.

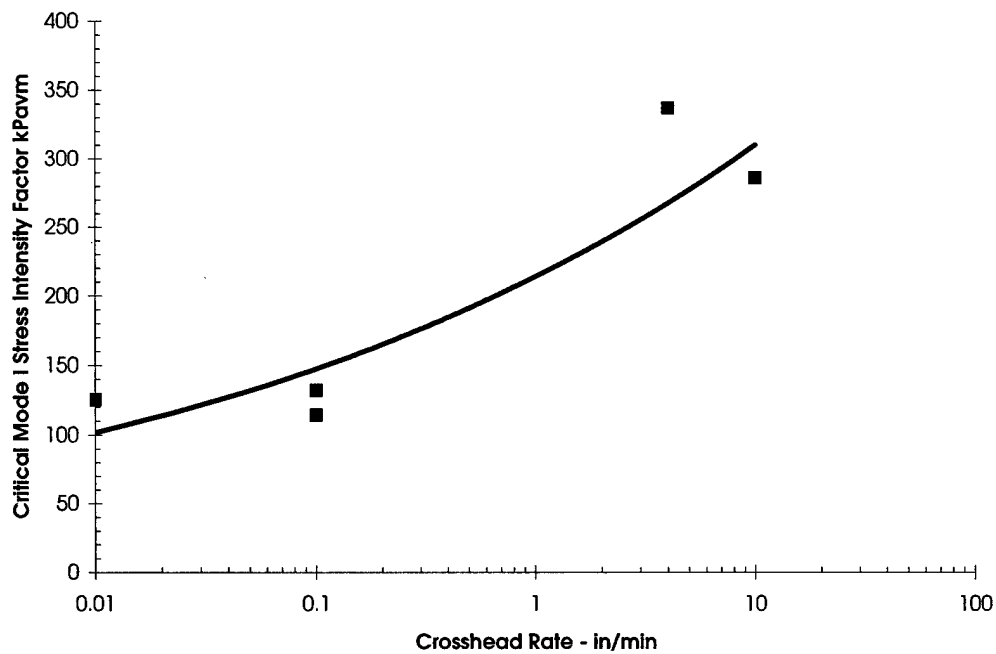


Figure 3. Dependence of the mode-I fracture toughness on the loading rate.

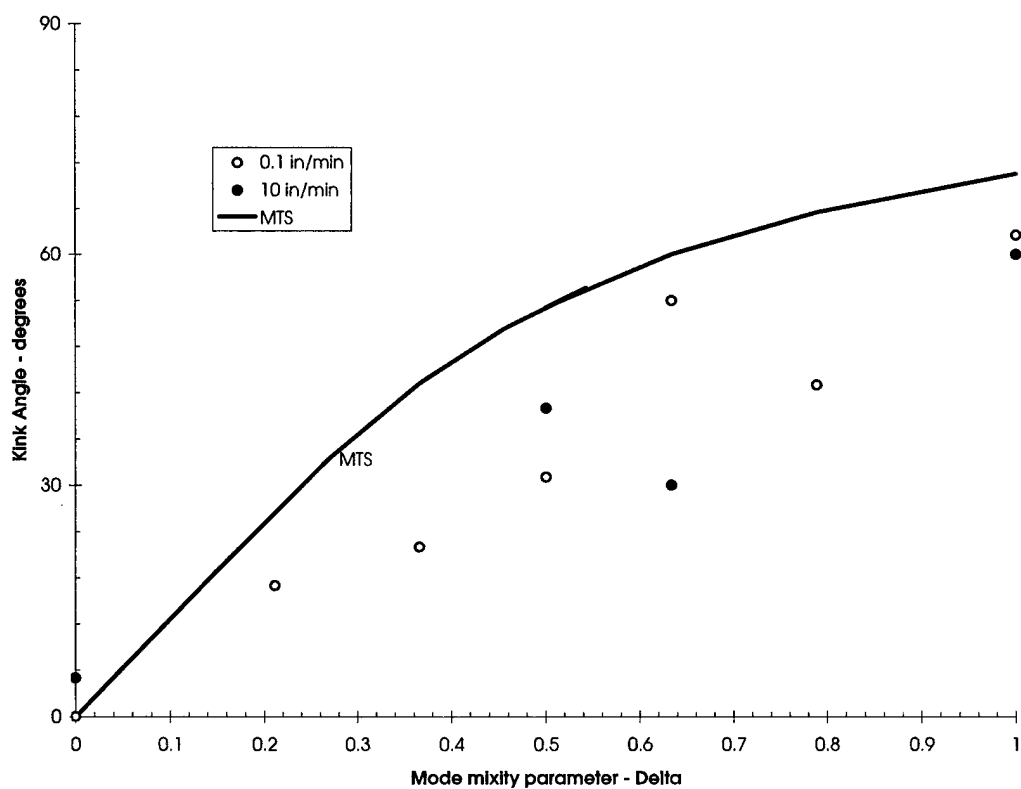


Figure 4. Measured variation of the crack kinking angle with the mode mixity parameter  $\delta = \mu/(1+\mu)$ . Predictions of the MTS theory do not correspond to the experimental observations.

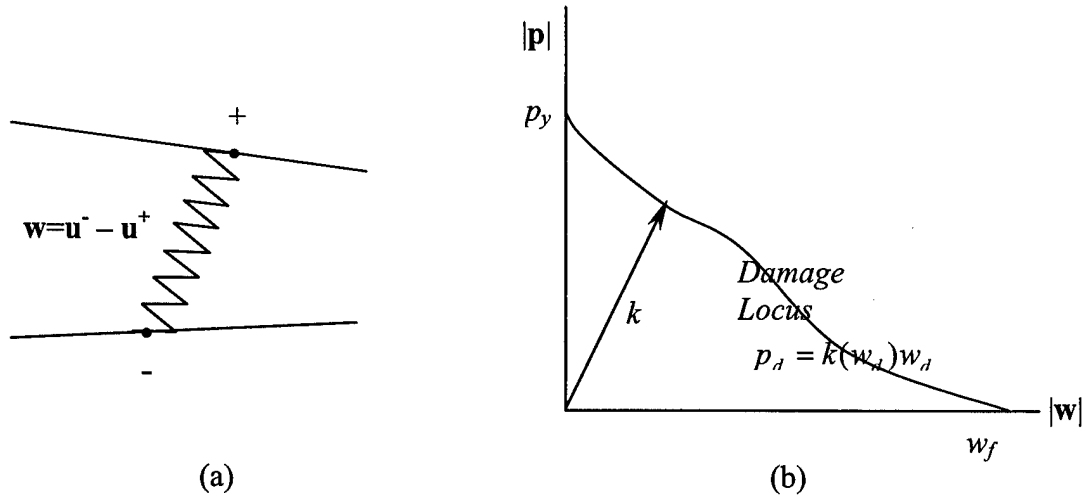


Figure 5. (a) Illustration of the two originally coincident points of a cohesive zone in the opening mode, connected by the line spring; (b) schematic diagram of the constitutive law of the line spring in terms of the traction and displacement jump. Note that instantaneous loading and unloading of the line spring is given by the slope  $k$ .

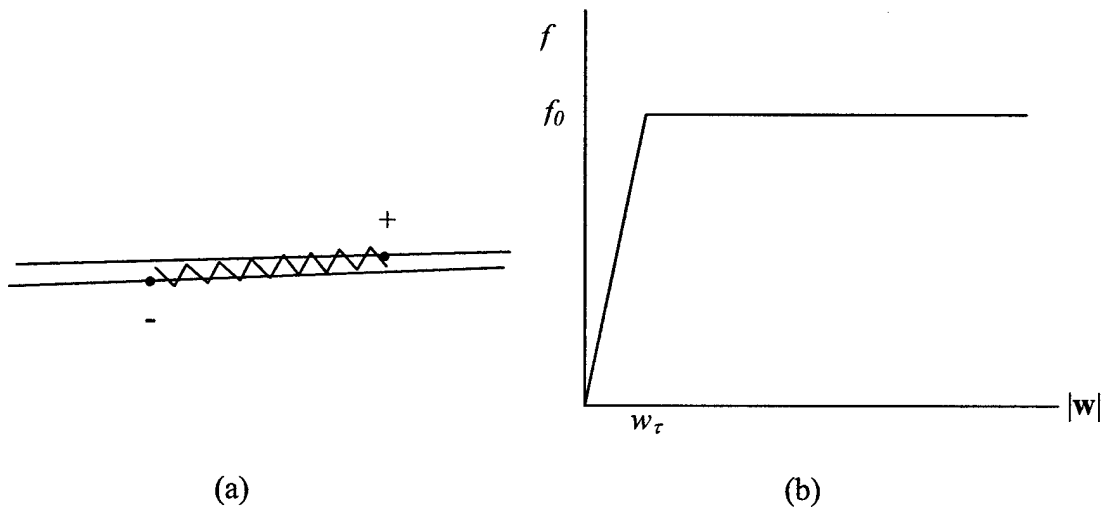


Figure 6. (a) Illustration of two originally coincident points of a cohesive zone in the contact/sliding mode. The tangential interaction between the two points is modeled using a Coulomb frictional force and the cohesive force, if the cohesive spring is not already broken. (b) Sketch of the variation of the frictional coefficient of the contact surface.

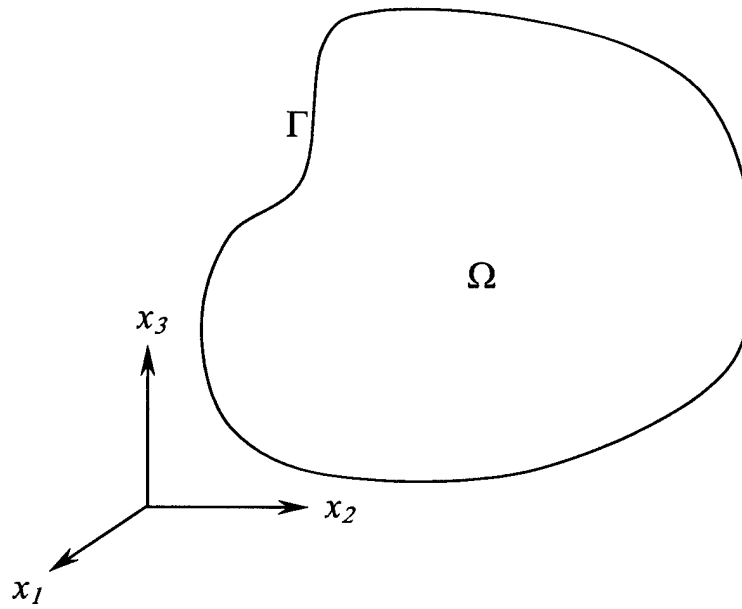


Figure 7 An isotropic, homogeneous, linear elastic domain  $\Omega$  with boundary  $\Gamma$ .

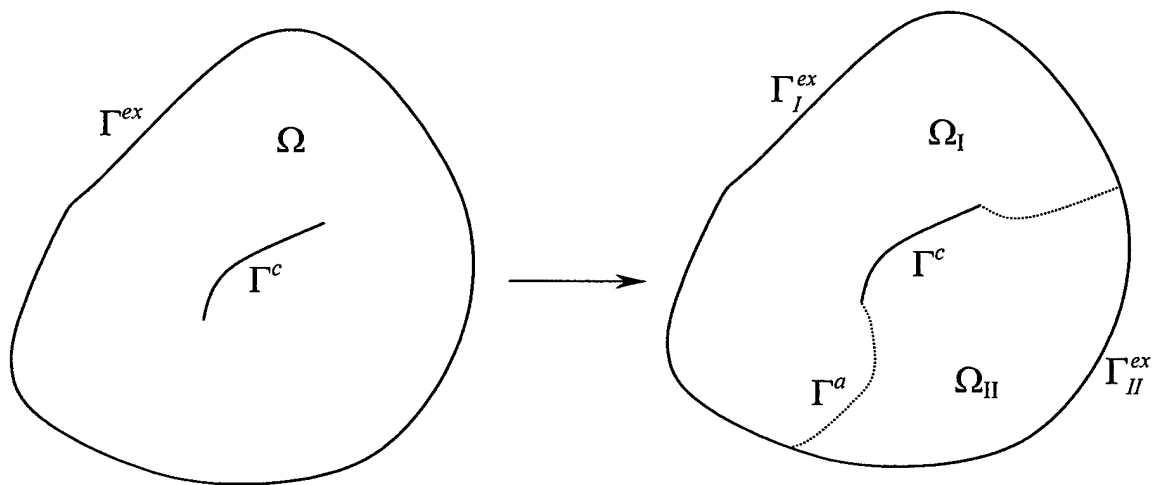


Figure 8. A domain  $\Omega$  containing a crack  $\Gamma^c$  is cut into two subdomains  $\Omega_I$  and  $\Omega_{II}$  along the dotted line path  $\Gamma^a$ .

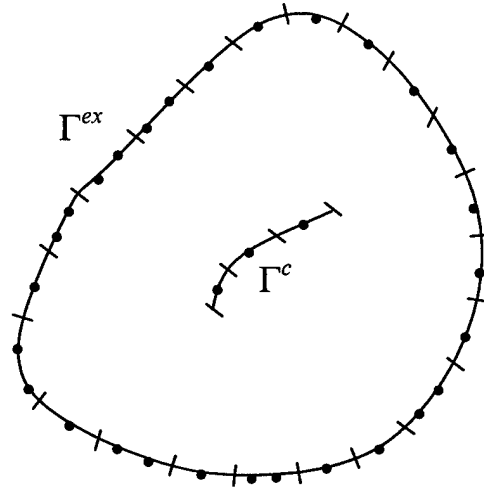


Figure 9. The discretization of the boundary into elements is shown in this figure. Each element contains one or more nodes distributed uniformly within the element. The nodes are internal to the element, indicating discontinuous elements.

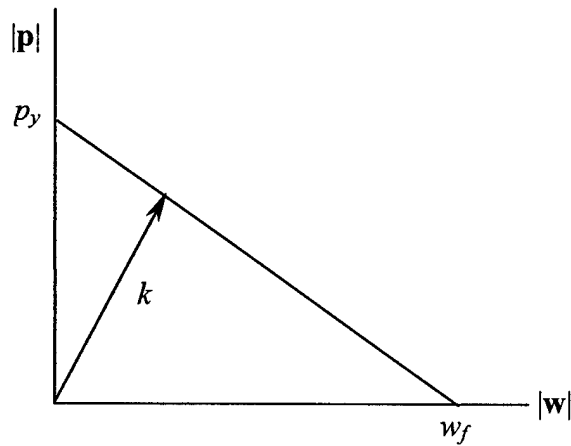


Figure 10. The two-parameter constitutive law for the cohesive zone material used in the simulations.



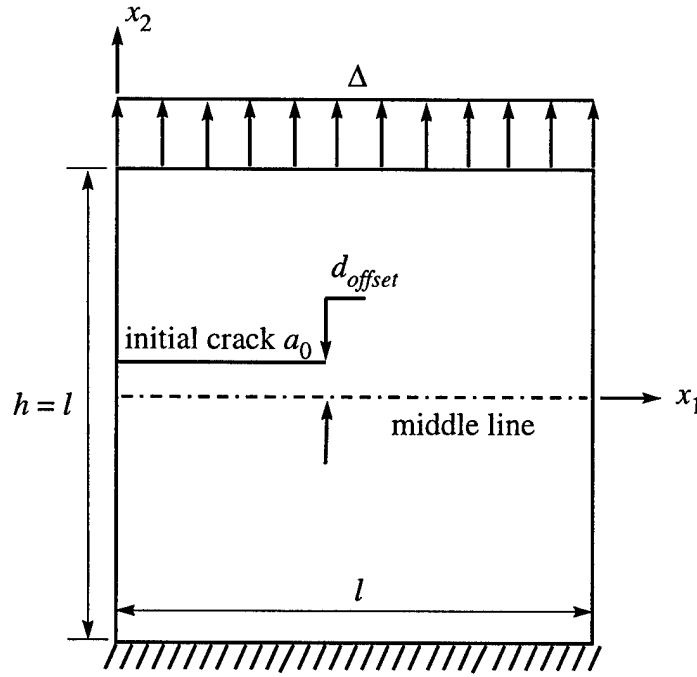


Figure 11. The configuration of a rectangular specimen with a single edge crack of initial length  $a_0$ , under displacement controlled elongation. This initial crack is parallel to the loading boundaries, and may be offset from the symmetry line in a distance.

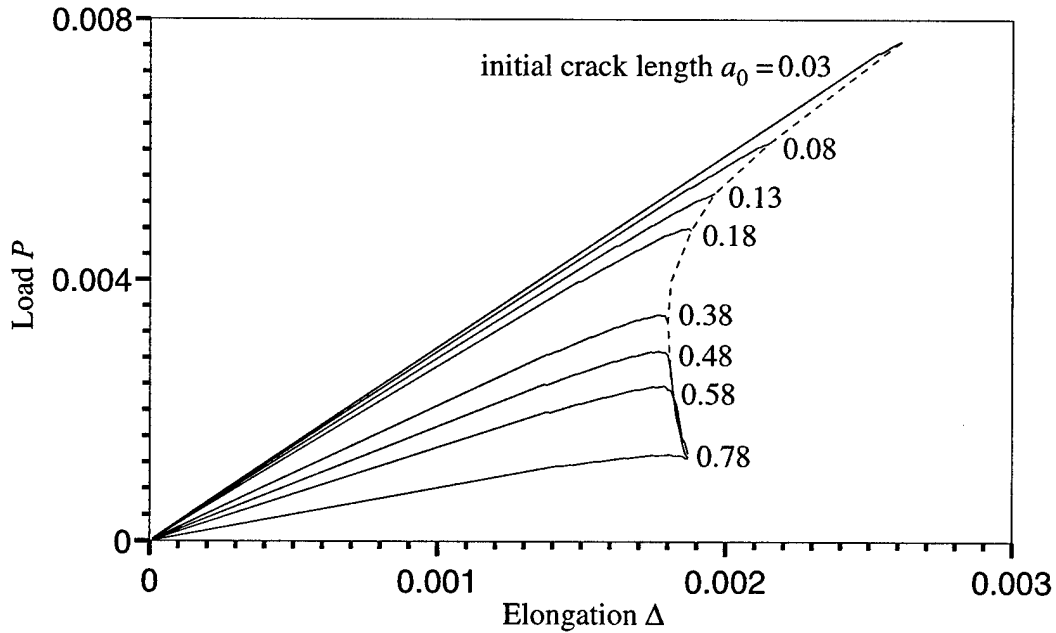


Figure 12. Load-elongation diagram of a set of simulations with a crack initially lying on  $x_2 = 0$  and with a length  $a_0$  from 0.03, to 0.78. An initial cohesive zone of size 0.02 is assumed in all the simulations. The crack growth is in the pure mode I. For  $a_0 < 0.48$  approximately, crack extension is unstable under displacement control.

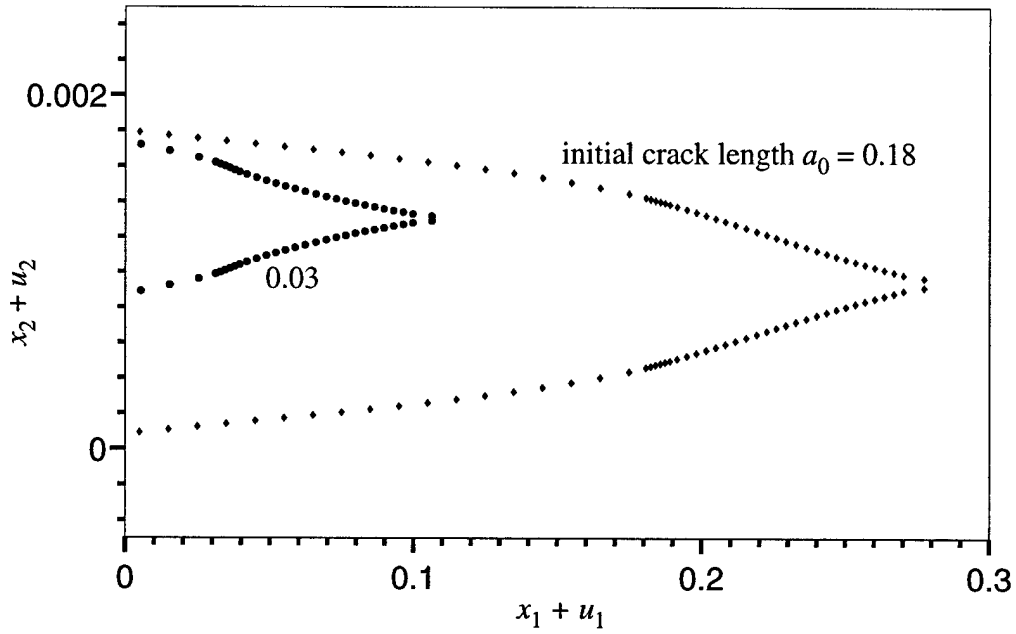


Figure 13. Crack opening profiles at the critical point of instability in two of the simulations for  $a_0 = 0.03$  and  $0.18$ .

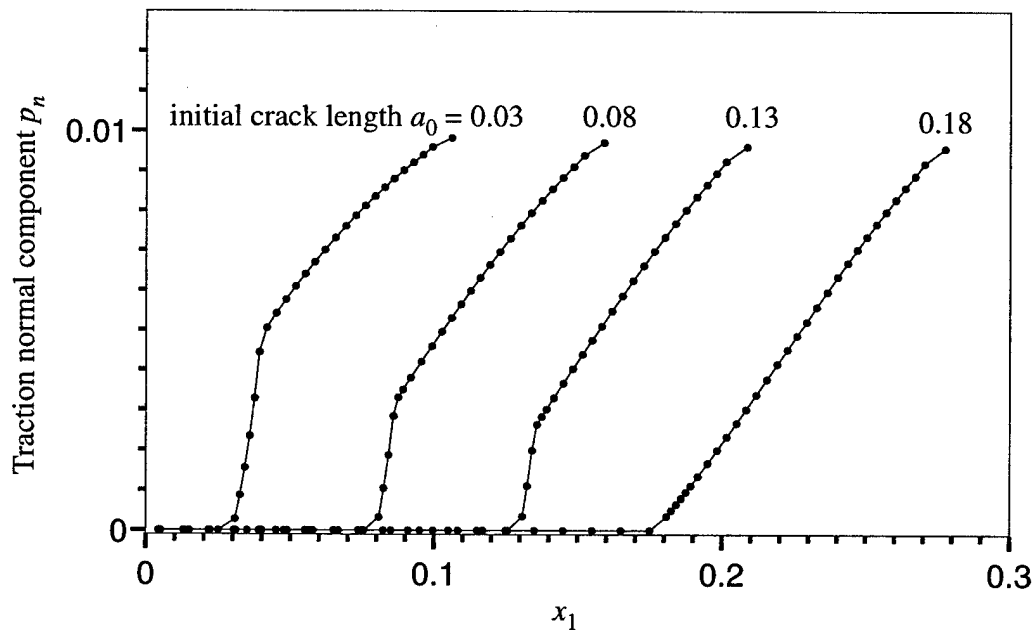


Figure 14. Traction normal component  $p_n$  along the cohesive zone at the critical point of instability in four of the simulations for  $a_0 = 0.03, 0.08, 0.13$ , and  $0.18$ . The tangential component is zero indicating a pure opening mode for the cohesive zone. Note that, for very short initial crack lengths, the cohesive zones are not fully developed.

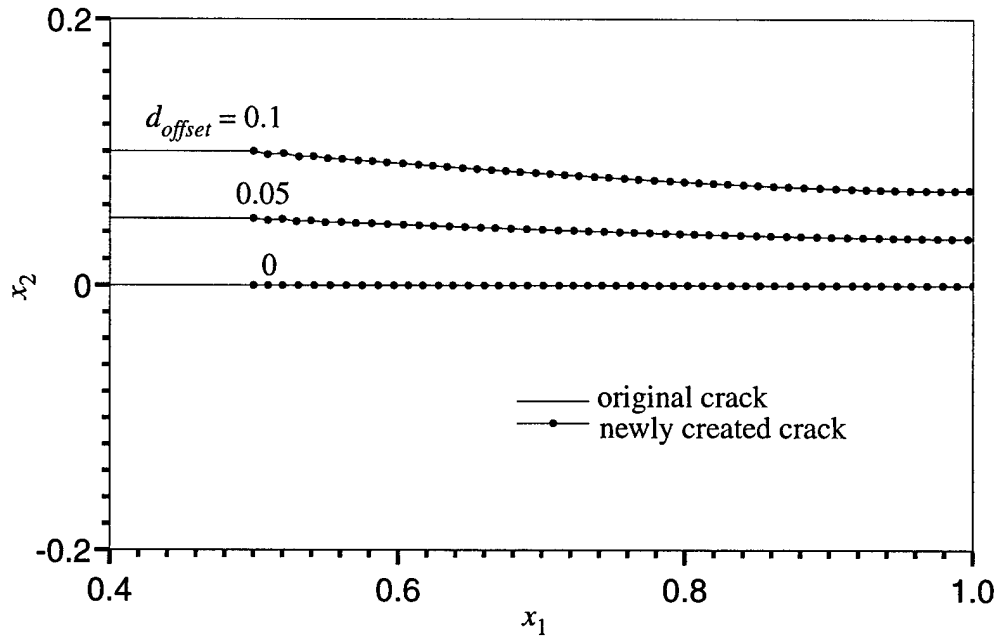


Figure 15. Crack trajectories in the simulations with different offsets of initial cracks. Nodes along the newly-created cracks are indicative of the new crack element ends.

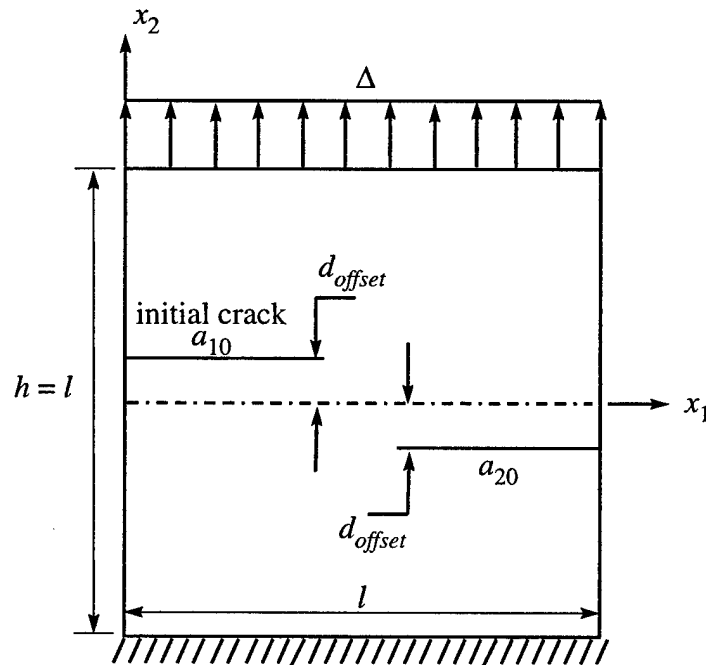


Figure 16. The loading configuration of a rectangular specimen with two edge cracks on the opposite sides, under displacement controlled elongation. The cracks are initially parallel to the loading boundaries, and may be offset from the symmetry line by a offset  $d_{offset}$ .

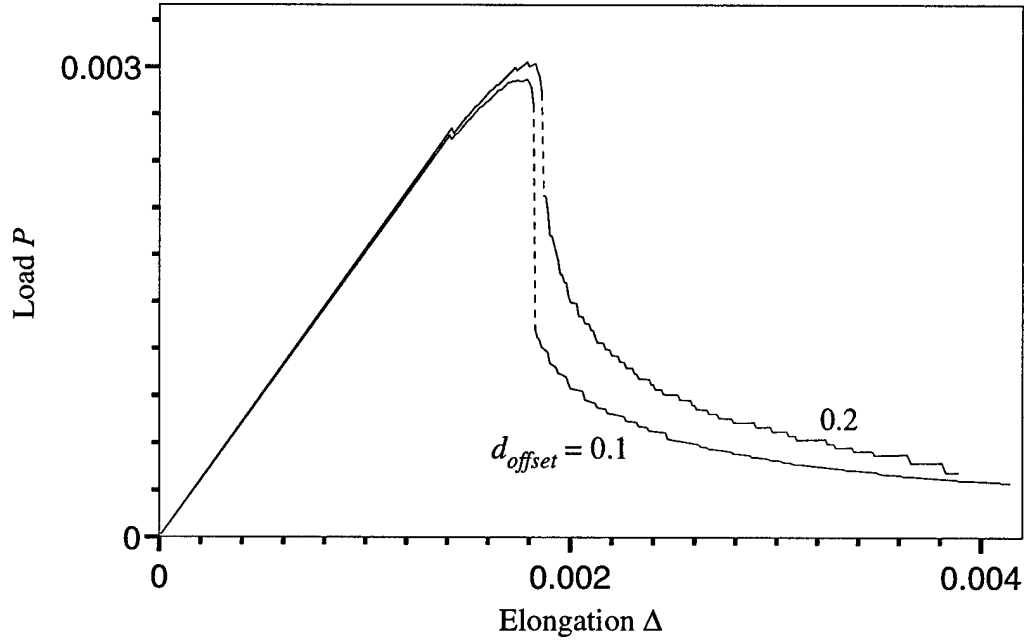


Figure 17. Load-elongation curves in the simulations of crack interaction with the offset  $d_{offset}$  as given above. Besides, the cracks  $a_{10} = a_{20} = 0.28$  initially, and each crack tip was assumed to have an initial cohesive zone of size 0.02. The dashed lined indicate the loss of structural stability.

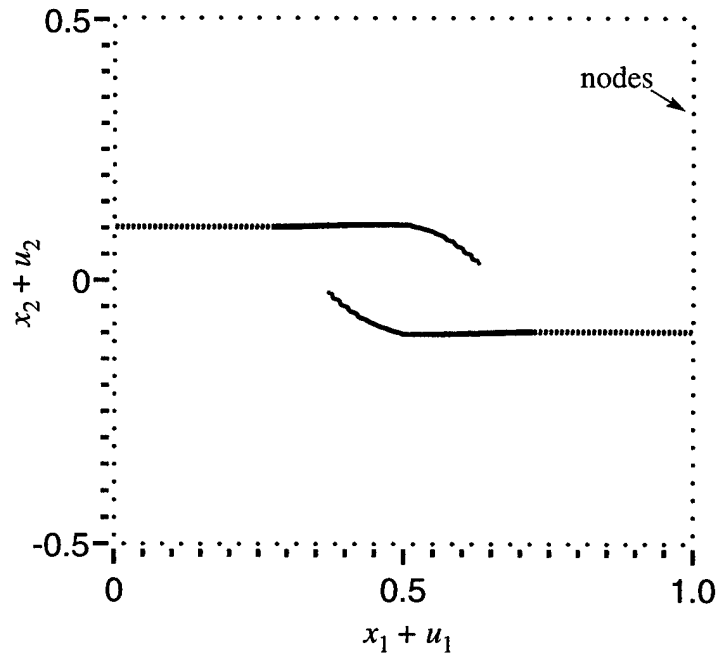


Figure 18. Deformed configuration of the specimen with two edge cracks with the offset  $d_{offset} = 0.1$ , corresponding to an extension  $\Delta = 0.0038$ .

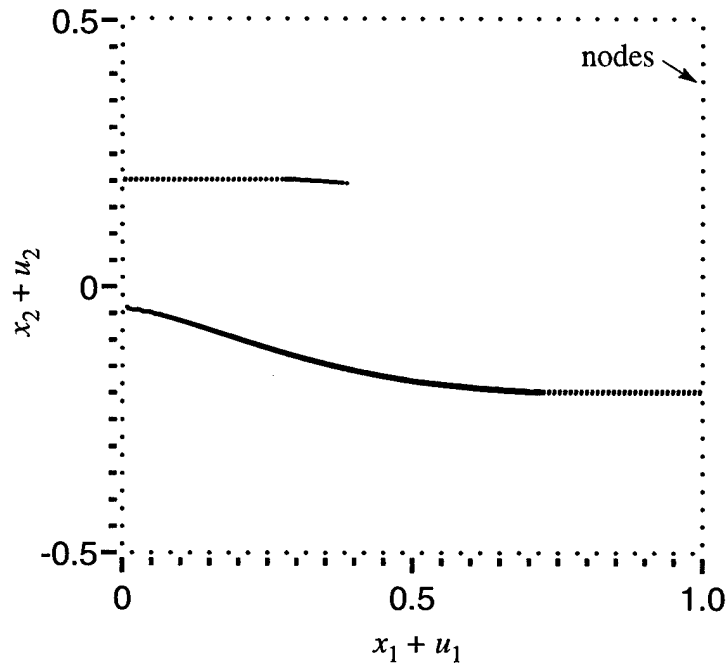


Figure 19. Deformed configuration of the specimen with two edge cracks with the offset  $d_{offset} = 0.2$ , corresponding to an extension  $\Delta = 0.0038$ .

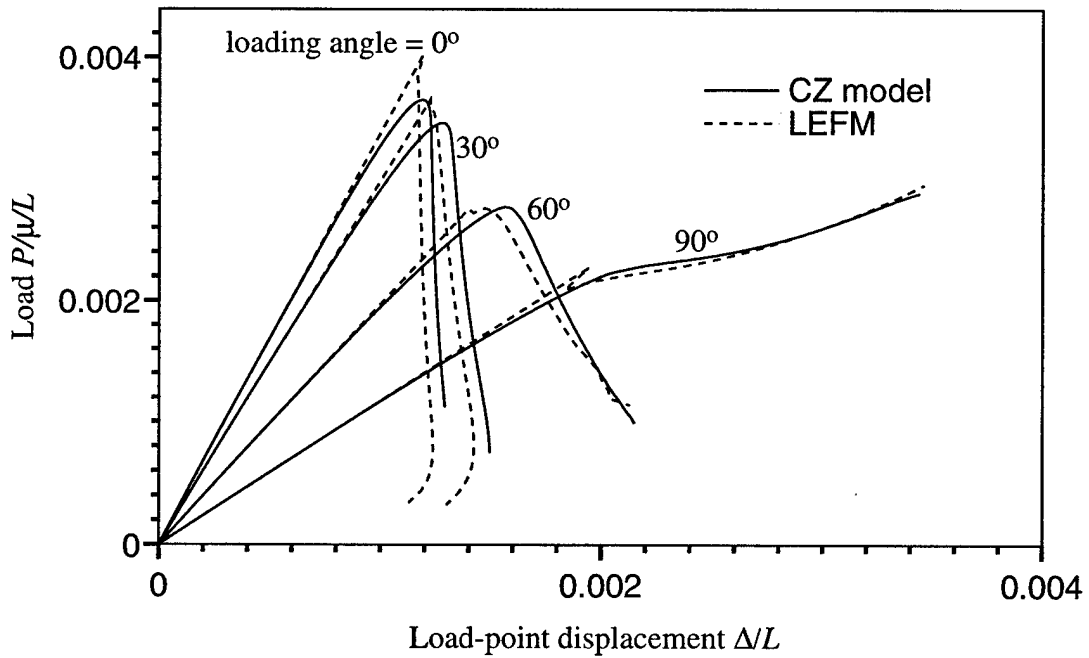


Figure 20 Load-load point displacement variation for mixed-mode crack growth, showing a comparison of the predictions of LEFM and the cohesive zone model.

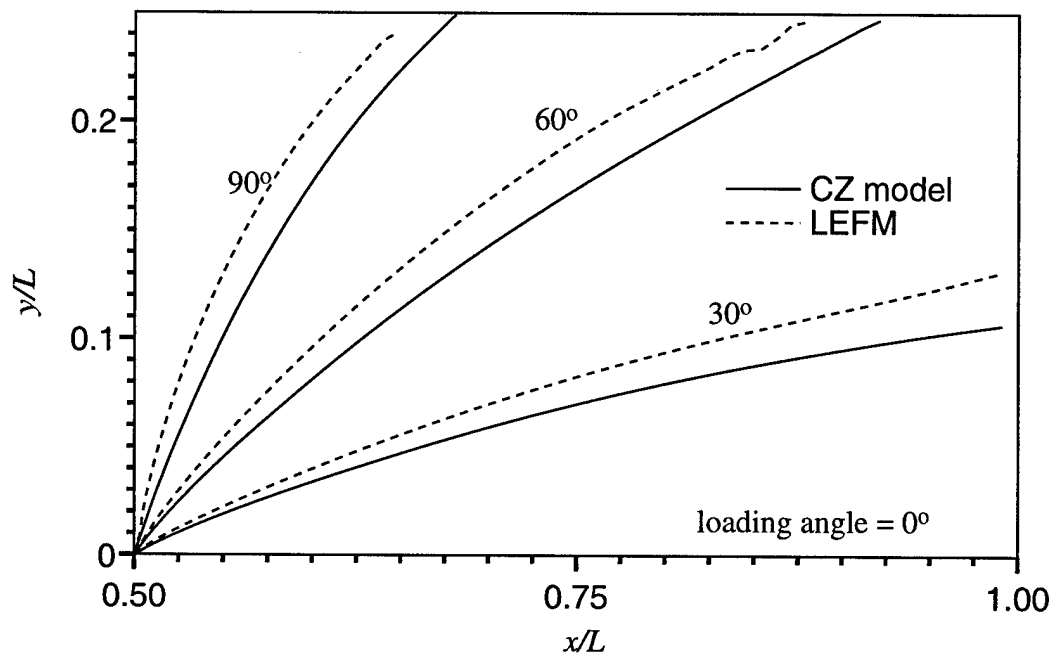


Figure 21. Comparison of the crack path predicted by the maximum tangential stress criterion and the cohesive zone model.

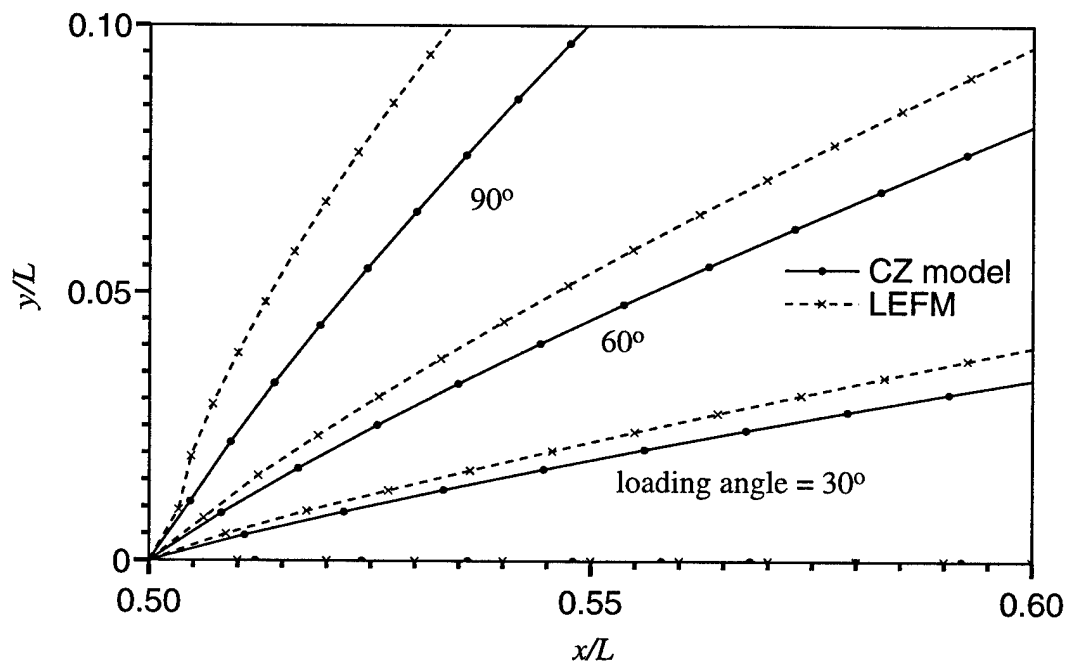


Figure 22. Comparison of the crack path predicted by LEFM and the cohesive zone model; only the region near the initial crack is shown.